drones

MDPI

Article

Capability-Aware Hierarchical Control with Priority-Based Lateral Recovery for Deadline-Guided Fixed-Wing UAV Formation Tracking

Xiuyuan Feng [1], Hao Cheng [1,2,*], Hua Wang [1], Xudong Xie [3], Wei Wei [1], Tao Han [1] and Siyuan Liu [1]

1 School of Astronautics, Beihang University, Beijing 102206, China; by2015117@buaa.edu.cn (X.F.); whua402@163.com (H.W.); weiwei1996@buaa.edu.cn (W.W.); tao_itimes@buaa.edu.cn (T.H.); sy2315106@buaa.edu.cn (S.L.)
2 State Key Laboratory of High-Efficiency Reusable Aerospace Transportation Technology, Beijing 102206, China
3 College of Mechanical and Electrical Engineering, Nanjing University of Aeronautics and Astronautics, Nanjing 210016, China; xxd0520@nuaa.edu.cn
* Correspondence: chenghao_1030@buaa.edu.cn

Highlights

What are the main findings?

- A capability-aware executable-boundary recovery controller (CAEBR) is proposed for deadline-guided fixed-wing UAV formation tracking under nonholonomic coupling, input saturation, and time-varying uncertainties.
- CAEBR separates the mission-level nominal deadline boundary from the control-layer executable boundary. Simulations show zero executable-boundary exceedance and improved lateral nominal-boundary re-entry under capability-limited conditions.

What are the implications of the main findings?

- The proposed method provides a feasible way to handle temporary mismatch between prescribed mission deadlines and real-time maneuvering capability, avoiding the unrealistic assumption that nominal performance boundaries are always enforceable.
- The priority-based lateral recovery strategy improves formation tracking reliability for fixed-wing UAVs, especially in the indirectly actuated lateral channel, while preserving bounded closed-loop behavior and heading-support feasibility.

Abstract

This paper studies deadline-guided formation tracking for fixed-wing unmanned aerial vehicles subject to nonholonomic coupling, input saturation, and time-varying uncertainties. The central difficulty is that the mission layer prescribes a nominal deadline-guided performance boundary, whereas the control layer may be temporarily unable to enforce it because the available maneuvering capability varies online. To address this mismatch, a capability-aware executable-boundary recovery controller, abbreviated as CAEBR, is developed. CAEBR distinguishes between a nominal deadline boundary and an executable boundary; the latter is adjusted according to online estimates of maneuvering capability and is recovered toward the nominal boundary when sufficient authority becomes available. The architecture contains three components: a bounded fast layer for executable-boundary regulation, priority-based lateral recovery, and matched residual compensation; a slow residual-aware predictive coordination layer for boundary recovery and heading-authority adjustment; and an adaptive residual-information layer for matched residual estimation and conservative residual-load indication. The fast-layer feedback uses bounded transformed-error terms, thereby avoiding circular boundedness arguments caused by unbounded commands under input saturation. Under admissible coordination, conservative

Check for updates

Academic Editor: Nadjim Horri

Received: 10 May 2026
Revised: 7 July 2026
Accepted: 10 July 2026
Published: 12 July 2026

 https://doi.org/10.3390/drones10070530

residual-load, and saturation-compatible executability conditions, the analysis establishes forward invariance of the executable boundary and heading-support tube, boundedness of closed-loop signals, and conditional recovery of the nominal boundary. Simulations demonstrate effective deadline-guided formation tracking, capability-dependent boundary relaxation under saturated recovery, improved lateral tracking in the more demanding scenario, Aerosonde-class 6-DoF command-execution consistency, and the remaining performance limitations when the selected executable-boundary budget is insufficient to remove all exceedance.

Keywords: fixed-wing UAV formation control; deadline-guided tracking; prescribed performance; hierarchical control; executable-boundary recovery

1. Introduction

Unmanned aerial vehicle (UAV) formation flight has attracted considerable attention because it can improve mission efficiency, sensing coverage, and operational robustness in surveillance, reconnaissance, environmental monitoring, search and rescue, and cooperative transportation tasks [1–3]. Among various UAV platforms, fixed-wing UAVs are particularly suitable for long-endurance and large-area missions because of their high aerodynamic efficiency, fast cruising speed, and long range [4,5]. However, compared with multirotor UAVs and simplified double-integrator agents, fixed-wing UAVs are subject to nonholonomic motion constraints, minimum-speed requirements, limited turning radius, input saturation, and strong longitudinal–lateral coupling [6–8]. These characteristics make deadline-guided formation tracking challenging, especially when transient performance requirements, limited maneuvering authority, and external disturbances must be considered simultaneously.

Formation-control methods for UAVs and multi-agent systems have been extensively investigated. Consensus-based and graph-theoretic methods provide effective tools for distributed coordination [9,10], while leader–follower and virtual-structure strategies offer intuitive formation specifications for cooperative motion generation [11–13]. Behavior-based and artificial-potential-field methods have also been used for formation maintenance, obstacle avoidance, and cooperative maneuvering [14,15]. For example, finite-time formation control with input saturation and dynamic leaders has been studied in [16], and artificial-potential-field-based multi-UAV obstacle avoidance and formation control has been investigated in [17]. Although these methods improve formation integrity and convergence performance, many of them are developed for general multi-agent systems, quadrotor platforms, or simplified agent models. Their direct application to fixed-wing formations is limited because the lateral tracking error is not directly actuated and must be reduced indirectly through heading adjustment and forward motion.

Formation control specifically for fixed-wing UAVs has therefore received increasing attention. Heintz et al. [18] developed an extended-unicycle-based formation controller for autonomous fixed-wing air vehicles with strict speed constraints. Li et al. [19] investigated affine formation tracking for fixed-wing UAVs with asymmetric speed constraints. Yu et al. [20] developed an event-triggered coordinated formation controller for fixed-wing UAVs under nonlinear external disturbances and wake-vortex effects. Liu et al. [21] studied centralized formation keeping for fixed-wing UAV flocking using reinforcement learning. Recent fixed-wing formation studies therefore cover strict speed constraints, asymmetric vehicle constraints, nonlinear disturbances, wake-vortex effects, learning-based coordination, and prescribed-performance or predefined-time tracking [18–26]. These studies have significantly advanced fixed-wing UAV formation control. Several recent fixed-wing studies are especially relevant as state-of-the-art references for benchmarking and positioning: adaptive predefined-time prescribed-performance path following [22], fixed-time optimal fault-tolerant prescribed-performance formation under dual faults [23], bearing-based fault-tolerant prescribed-performance formation [24], distributed robust adaptive practical finite-time formation tracking [25], and prescribed-time formation tracking with disturbances and failures [27]. These works provide stronger modern fixed-wing control references than generic mechanism-level baselines alone. However, most of them enforce a fixed task boundary or improve tracking robustness under assumed admissible command authority. They do not explicitly model the case in which a deadline-induced performance boundary is temporarily beyond the instantaneous maneuvering capability and must be converted into a recoverable executable boundary. Accordingly, the present paper uses these studies to position the benchmark classes and contribution boundary, while avoiding an unsupported claim that all modern fixed-wing controllers are fully reproduced under identical inner-loop, fault, communication, and platform assumptions.

To improve transient tracking performance, prescribed-performance control [22–24], finite-time control [25,28], fixed-time control [29,30], and prescribed-time control [31,32] have been introduced into nonlinear tracking and formation-control problems. Classical funnel-control and prescribed-performance adaptive-control results further show how tracking errors can be constrained by time-varying funnels or envelopes [33–35]. These methods can constrain tracking errors within predefined performance envelopes or guarantee convergence within a specified time, making them attractive for time-critical UAV missions. For fixed-wing UAVs, Zheng et al. [26] proposed a prescribed-time maneuvering-target-closing method for multiple fixed-wing UAVs. Recent multi-agent studies have also extended fixed- or preassigned-time regulation to heterogeneous signed networks [36]. However, most prescribed-performance, prescribed-time, and funnel-type designs implicitly assume that the prescribed boundary or convergence requirement is always enforceable by the available control authority. For constrained fixed-wing UAVs, this assumption may fail when the nominal deadline boundary becomes too tight relative to the instantaneous maneuvering capability, particularly during large-initial-error recovery, aggressive turning maneuvers, or input saturation. These single-envelope designs usually do not provide an online mechanism that records the temporary gap between the mission-level boundary and the boundary enforceable by the saturated aircraft. Therefore, a deadline boundary should not only specify the desired transient performance but also be coordinated with real-time executable capability.

Input constraints are central to this executability issue. Saturation-aware control, anti-windup compensation, command filtering, and dynamic surface control can mitigate the adverse effects of input constraints [37–40], while model predictive control provides a systematic way to handle state and input constraints in trajectory tracking and cooperative control [41–43]. Robust and tube-based predictive control methods further improve constraint satisfaction under bounded disturbances and model uncertainty [44,45]. Learning-based flight-control studies have also addressed state/input constraints or complex morphing dynamics using safe reinforcement learning or convex-combined deep reinforcement learning schemes [46,47]. Nevertheless, in many constrained-control designs, relaxation or constraint tightening is mainly used as a numerical feasibility or robustness device. It is rarely interpreted as a physical performance–capability coordination variable that quantifies the temporary gap between mission-level deadline requirements and real-time maneuvering authority.

Disturbance rejection, adaptive residual compensation, and safety-critical control are also closely related to constrained transient formation tracking. Disturbance observers, extended state observers, adaptive estimators, and learning-based residual models can improve robustness by estimating or compensating for unknown disturbances [48–50]. A recent fixed-wing formation-control study also developed a distributed finite-time ESO consensus controller for multiple fixed-wing UAVs under external disturbances [20], and observer-based secure consensus has further been investigated for multi-agent systems under multimode denial-of-service attacks [51]. However, aggressive residual cancellation may amplify estimation errors or observer transients. Moreover, for fixed-wing UAVs, lateral residual effects cannot be cancelled in the same direct manner as matched longitudinal or heading-channel disturbances because the lateral channel is indirectly actuated. Meanwhile, invariant-set methods, barrier Lyapunov functions, and control barrier functions provide useful tools for maintaining state constraints and ensuring forward invariance [52–54]. Yet most of these methods focus on enforcing a fixed admissible set or prescribed safety boundary. These recent works highlight time-critical, constrained, intelligent, observer-based, and secure cooperative-control directions, but they do not specifically resolve deadline-boundary executability for saturated fixed-wing formations. In deadline-guided fixed-wing formation tracking, the critical issue is that the nominal performance boundary may become temporarily infeasible and should be recovered only when sufficient maneuvering capability becomes available. Accordingly, the reviewed literature leaves mechanism-level and recent fixed-wing alternatives that are closest to the present objective: fixed prescribed-boundary enforcement, prescribed-time prescribed-performance single-envelope enforcement, disturbance-compensated robust tracking, finite-time ESO-based consensus tracking, and optimization-based constrained tracking. These alternatives motivate the PPC, PT-PPC, DOB, FT-ESO, and MPC baselines used in the simulation study, with PT-PPC added as an advanced prescribed-time single-envelope comparator and FT-ESO added as a recent fixed-wing observer/consensus comparator. The baseline comparison is not intended to claim that these implementations exhaust all state-of-the-art fixed-wing formation controllers. Rather, it is designed to test whether CAEBR adds a capability-aware recovery function beyond the most relevant competing mechanisms: prescribed-boundary tracking, prescribed-time single-envelope tracking, residual compensation, finite-time ESO-based consensus tracking, and soft-constrained receding-horizon control.

Motivated by the above observations, this paper studies deadline-guided formation tracking for fixed-wing UAVs subject to nonholonomic coupling, input saturation, and time-varying uncertainties. The key difficulty lies in the mismatch between mission-level deadline requirements and the real-time maneuvering capability of constrained fixed-wing platforms. If this mismatch is ignored, the controller may generate excessive saturation, poor transient recovery, or ineffective boundary regulation, especially in the lateral channel where error reduction depends indirectly on heading adjustment.

To address this problem, a capability-aware executable-boundary recovery controller (CAEBR) is developed. CAEBR separates the nominal deadline boundary from the executable boundary enforced by the control layer and coordinates the gap between them according to online maneuvering capability. A priority-based lateral recovery mechanism is further introduced to strengthen nominal-boundary re-entry when the lateral channel becomes critical and sufficient turning margin is available.

The main contributions are summarized as follows.

1. A capability-aware deadline-guided formation-control formulation is developed for fixed-wing UAVs under nonholonomic motion, input saturation, and time-varying disturbances. By introducing both a nominal deadline boundary and an executable boundary, CAEBR explicitly separates mission-level transient-performance requirements from real-time control feasibility constraints.

2. A capability-aware executable-boundary recovery mechanism is developed rather than treating constraint relaxation as a purely numerical slack variable. The relaxation variables are driven by online maneuvering-capability and residual-load information, enter the enforced transformed-error boundary directly, and are recovered toward zero when sufficient authority returns. The fast, slow, and adaptive components are used as implementation layers for this mechanism, rather than being claimed as independent sources of novelty.
3. A priority-based lateral recovery augmentation mechanism is designed for the under-actuated lateral channel. When the lateral transformed error approaches or exceeds the nominal boundary and sufficient turning margin is available, the mechanism increases lateral recovery priority through enhanced virtual-heading correction and moderated longitudinal feedback, thereby promoting nominal-boundary recovery without sacrificing executable-boundary feasibility.
4. A stability, invariance, and conditional-recovery analysis is provided. Under saturation-compatible executable-boundary conditions, CAEBR guarantees forward invariance of the executable boundary and heading-support tube, boundedness of closed-loop signals, and recovery of the executable boundary toward the nominal deadline boundary when sufficient capability is restored.

The remainder of this paper is organized as follows. Section 2 presents the fixed-wing formation model and problem formulation. Section 3 develops CAEBR, including fast executable-boundary tracking, priority-based lateral recovery, slow predictive coordination, and adaptive residual-information construction. Section 4 presents simulation studies. Section 5 discusses practical implementation and limitations. Section 6 concludes this paper. Appendix A provides stability, invariance, and recoverability analysis.

2. System Model and Problem Formulation

2.1. Fixed-Wing UAV Kinematics

Consider a leader–follower formation composed of one leader denoted by A_0 and N followers denoted by A_i, $i = 1, \ldots, N$. The state of follower i is described by

$$q_i = [x_i,\ y_i,\ \theta_i]^\top, \tag{1}$$

where $(x_i, y_i) \in \mathbb{R}^2$ denotes the inertial position and $\theta_i \in \mathbb{R}$ is the heading angle.

The planar kinematics are modeled as

$$\begin{aligned} \dot{x}_i &= v_i \cos\theta_i + d_{x,i}, \\ \dot{y}_i &= v_i \sin\theta_i + d_{y,i}, \\ \dot{\theta}_i &= \omega_i + d_{\theta,i}, \end{aligned} \tag{2}$$

where v_i and ω_i denote the applied speed and turn-rate commands generated by the controller, and $d_{x,i}$, $d_{y,i}$, and $d_{\theta,i}$ denote lumped plant-level disturbances caused by wind and unmodeled effects.

The applied inputs of each fixed-wing aircraft are constrained by

$$v_{\min} \le v_i \le v_{\max}, \qquad |\omega_i| \le \omega_{\max}, \tag{3}$$

where $0 < v_{\min} < v_{\max}$ and $\omega_{\max} > 0$. Equation (2) is an outer-loop kinematic model. The controller does not directly command aerodynamic surfaces; instead, v_i and ω_i are interpreted as speed and turn-rate references tracked by a lower-level fixed-wing autopilot. The saturation limits in Equation (3) should therefore be chosen within the physical envelope of the aircraft and its inner-loop controller. For a coordinated level turn, $|\omega_i|$

is related to the bank angle ϕ_i approximately by $|\omega_i| = g|\tan\phi_i|/v_i$, and the load factor satisfies $n_i = 1/\cos\phi_i$. Thus, $\omega_{\max}$ should be no larger than the turn-rate permitted by the allowable bank angle and load factor over the operating speed interval. Any residual inner-loop tracking error, wind-induced drift, or unmodeled aerodynamic effect is included in the lumped disturbance terms in Equation (2).

The leader state $q_0 = [x_0, y_0, \theta_0]^\top$ and its input signals v_0, ω_0 are assumed to be measurable through onboard sensing or communication.

Assumption 1. *The leader signals are bounded and piecewise continuously differentiable. Specifically, there exist positive constants $\bar{v}_0, \bar{\omega}_0, \bar{a}_0, \bar{\alpha}_0$ such that*

$$|v_0(t)| \le \bar{v}_0, \quad |\omega_0(t)| \le \bar{\omega}_0, \quad |\dot{v}_0(t)| \le \bar{a}_0, \quad |\dot{\omega}_0(t)| \le \bar{\alpha}_0, \tag{4}$$

for all $t \ge 0$.

Assumption 2. *For each follower i, the plant-level lumped disturbances in Equation (2) are bounded and have bounded variation rates, i.e.,*

$$|d_{j,i}(t)| \le \bar{d}_{j,i}^{\mathrm{phys}}, \qquad |\dot{d}_{j,i}(t)| \le \bar{l}_{j,i}, \qquad j \in \{x, y, \theta\}, \tag{5}$$

where $\bar{d}_{j,i}^{\mathrm{phys}} > 0$ and $\bar{l}_{j,i} > 0$ are finite but unknown constants.

2.2. Formation Error Dynamics

The geometric relationship among the leader, follower i, its desired formation position, the body-frame errors, and the heading-support direction is illustrated in Figure 1.

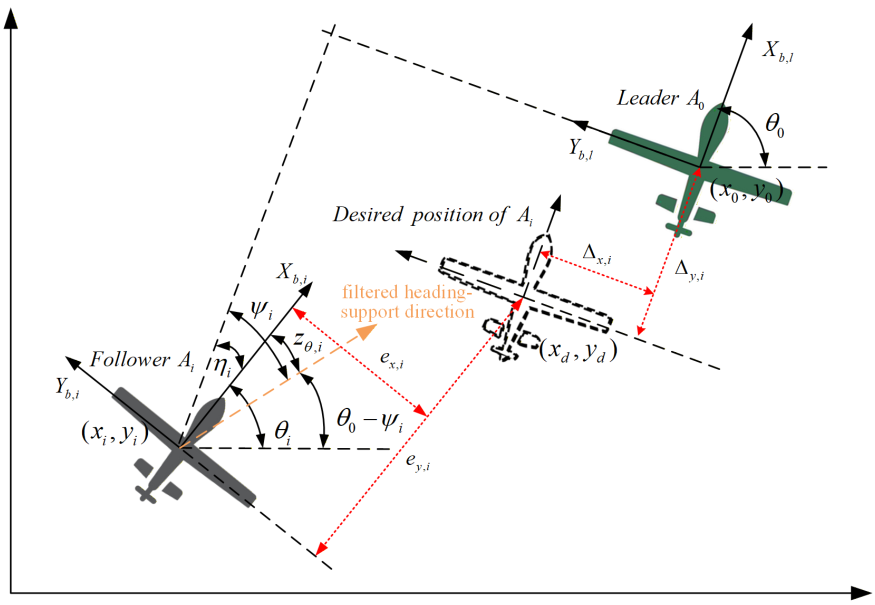

Figure 1. Planar fixed-wing formation geometry.

For a prescribed formation pattern, let the desired offset of follower i in the leader body frame be

$$\Delta_i = [\Delta_{x,i},\ \Delta_{y,i}]^\top. \tag{6}$$

Then the desired inertial reference position is

$$p_{d,i} = \begin{bmatrix} x_{d,i} \\ y_{d,i} \end{bmatrix} = \begin{bmatrix} x_0 \\ y_0 \end{bmatrix} + R(\theta_0)\Delta_i, \tag{7}$$

where

$$R(\theta) = \begin{bmatrix} \cos\theta & -\sin\theta \\ \sin\theta & \cos\theta \end{bmatrix}. \tag{8}$$

Differentiating Equation (7) gives

$$\dot{p}_{d,i} = \begin{bmatrix} v_0 \cos\theta_0 \\ v_0 \sin\theta_0 \end{bmatrix} + \omega_0 R(\theta_0) \begin{bmatrix} -\Delta_{y,i} \\ \Delta_{x,i} \end{bmatrix}. \tag{9}$$

Define the position vector of follower i as $p_i = [x_i, y_i]^\top$. The formation tracking error expressed in the follower body frame is

$$e_i = \begin{bmatrix} e_{x,i} \\ e_{y,i} \end{bmatrix} = R^\top(\theta_i)(p_{d,i} - p_i), \tag{10}$$

where $e_{x,i}$ and $e_{y,i}$ denote the longitudinal and lateral tracking errors, respectively.

Define the relative heading

$$\eta_i = \theta_0 - \theta_i. \tag{11}$$

In fixed-wing formation tracking, η_i is not treated as a primary deadline-constrained performance variable. Instead, it is used as an auxiliary mechanism for supporting lateral error correction.

Let $\theta_{v,i}$ denote a virtual heading-correction signal to be designed in the fast layer. To avoid direct differentiation of the virtual heading signal, introduce the first-order filter

$$\tau_\psi \dot{\psi}_i + \psi_i = \theta_{v,i}, \qquad \tau_\psi > 0, \tag{12}$$

and define the heading-support error as

$$z_{\theta,i} = \psi_i - \eta_i. \tag{13}$$

Thus, ψ_i is the filtered virtual heading reference, while $z_{\theta,i}$ measures the deviation between the filtered heading-support signal and the relative-heading state.

Using Equations (2) and (11)–(13), the augmented formation-error dynamics can be written as

$$\begin{aligned}
\dot{e}_{x,i} &= v_0 \cos(\psi_i - z_{\theta,i}) - \omega_0 \Big(\Delta_{x,i} \sin(\psi_i - z_{\theta,i}) + \Delta_{y,i} \cos(\psi_i - z_{\theta,i}) \Big) - v_i + \omega_i e_{y,i} + \tilde{d}^e_{x,i}, \\
\dot{e}_{y,i} &= v_0 \sin(\psi_i - z_{\theta,i}) + \omega_0 \Big(\Delta_{x,i} \cos(\psi_i - z_{\theta,i}) - \Delta_{y,i} \sin(\psi_i - z_{\theta,i}) \Big) - \omega_i e_{x,i} + \tilde{d}^e_{y,i}, \\
\dot{z}_{\theta,i} &= \dot{\psi}_i - \omega_0 + \omega_i + \tilde{d}^z_{\theta,i}.
\end{aligned} \tag{14}$$

Here, $\tilde{d}^e_{x,i}$, $\tilde{d}^e_{y,i}$, and $\tilde{d}^z_{\theta,i}$ denote transformed lumped disturbances in the augmented error dynamics.

Equation (14) highlights the nonholonomic coupling intrinsic to fixed-wing motion. In particular, the lateral error $e_{y,i}$ is not directly actuated and must be corrected through heading adjustment and forward motion.

2.3. Deadline-Guided Performance Specification

For each follower i, the mission layer specifies a deadline $T^\star > 0$ and target radii $r_{x,i} > 0$, $r_{y,i} > 0$ for the longitudinal and lateral position errors. To encode this requirement in a bounded transformed domain, define for each position channel $j \in \{x, y\}$

$$h_j(e_{j,i}) = \tanh(\kappa_j e_{j,i}), \qquad \kappa_j > 0. \tag{15}$$

Given the target radius $r_{j,i}$, the corresponding terminal bound in the transformed domain is

$$\mu_{j,i}^{\infty} = \tanh(\kappa_j r_{j,i}) \in (0,1). \tag{16}$$

Let $\mu_{j,i}^{0} \in (\mu_{j,i}^{\infty}, 1)$ denote the initial allowable bound. The nominal deadline boundary is defined as

$$\mu_{j,i}^{\mathrm{nom}}(t) = \begin{cases} \mu_{j,i}^{\infty} + \left(\mu_{j,i}^{0} - \mu_{j,i}^{\infty}\right)\left(1 - \dfrac{t}{T^{\star}}\right)^{\ell_j}, & 0 \le t < T^{\star}, \\ \mu_{j,i}^{\infty}, & t \ge T^{\star}, \end{cases} \tag{17}$$

where $\ell_j > 1$ is a shape parameter. If the nominal boundary is satisfied for all $t \ge 0$, then

$$|e_{j,i}(t)| \le r_{j,i}, \qquad \forall t \ge T^{\star}. \tag{18}$$

The nominal boundary $\mu_{j,i}^{\mathrm{nom}}(t)$ characterizes the desired mission-layer transient requirement. However, for constrained fixed-wing UAVs subject to nonholonomic coupling, input saturation, and time-varying disturbances, this boundary may not always be directly enforceable in real time.

To accommodate a temporary capability shortage, an executable boundary is introduced:

$$\mu_{j,i}^{\mathrm{act}}(t) = \mu_{j,i}^{\mathrm{nom}}(t) + \delta_{j,i}(t), \qquad j \in \{x, y\}, \tag{19}$$

where $\delta_{j,i}(t) \ge 0$ is a capability-dependent relaxation variable. The executable-boundary requirement is

$$|h_j(e_{j,i}(t))| \le \mu_{j,i}^{\mathrm{act}}(t), \qquad j \in \{x, y\}. \tag{20}$$

Thus, $\mu_{j,i}^{\mathrm{nom}}(t)$ represents the deadline-guided task requirement, whereas $\mu_{j,i}^{\mathrm{act}}(t)$ represents the boundary that can be enforced in real time with the currently available maneuvering capability. The relaxation variable $\delta_{j,i}(t)$ is a control-layer executability indicator that quantifies the temporary gap between the mission-level demand and the available control authority.

Unlike a conventional soft-constraint slack used only inside an optimization cost, this relaxation variable is part of the closed-loop performance specification rather than merely a numerical feasibility device. It defines the boundary actually enforced by the controller, appears in the transformed-error normalization and invariance conditions, and is scheduled according to online maneuvering capability. Hence, the relaxation has a physical interpretation as the temporary capability gap between the nominal deadline requirement and the boundary that can be enforced by the saturated fixed-wing platform. This interpretation is operational rather than a first-principles aerodynamic derivation: the executable boundary is computed from the outer-loop saturation margins, residual-load indicators, and selected relaxation budget, and it should be calibrated against the physical speed, bank-angle, load-factor, and actuator limits of the specific airframe.

The executable boundary is initialized before the online coordination starts. Let

$$\eta_{j,i}^{0} = |h_j(e_{j,i}(0))|, \qquad j \in \{x, y\}. \tag{21}$$

Given a small margin $\varepsilon_{j,i}^{0} > 0$, the initial relaxation is selected as

$$\delta_{j,i}(0) = \Pi_{[0,\bar{\delta}_j]}\left(\eta_{j,i}^{0} + \varepsilon_{j,i}^{0} - \mu_{j,i}^{\mathrm{nom}}(0)\right), \tag{22}$$

where $\Pi_{[0,\bar{\delta}_j]}(\cdot)$ denotes projection onto the admissible interval. Therefore, if the initial error satisfies

$$\eta_{j,i}^{0} + \varepsilon_{j,i}^{0} \le \mu_{j,i}^{\mathrm{nom}}(0) + \bar{\delta}_j < 1, \tag{23}$$

then $|h_j(e_{j,i}(0))| < \mu_{j,i}^{\mathrm{act}}(0)$, and the transformed-error variables are well defined at the initial time. If Equation (23) is violated, the selected relaxation budget is insufficient to certify initial executable-boundary feasibility. In that case, either the admissible relaxation budget or the mission-level boundary must be enlarged by the task layer, or the invariance guarantee starts after a feasible executable boundary has been initialized.

Remark 1. *The introduction of the executable boundary does not change the mission requirement. The nominal boundary remains the task-level performance specification. The relaxation variable only indicates that the prescribed boundary is temporarily beyond the available maneuvering capability. In a complete autonomous mission architecture, this indicator may be reported to the task-planning layer for replanning or task reassignment. This paper focuses on the control-layer problem: during a temporary capability shortage, CAEBR preserves executable-boundary feasibility, keeps the formation bounded, and promotes recovery toward the nominal boundary once sufficient capability becomes available.*

2.4. Problem Formulation

The control problem is to design a hierarchical controller such that, for each follower i, the following objectives are achieved.

1. The transformed longitudinal and lateral position errors remain within the executable boundary for all $t \geq 0$:

$$|h_x(e_{x,i}(t))| \leq \mu_{x,i}^{\mathrm{act}}(t), \qquad |h_y(e_{y,i}(t))| \leq \mu_{y,i}^{\mathrm{act}}(t). \tag{24}$$

2. The heading-support channel remains bounded within a prescribed small-angle tube:

$$|z_{\theta,i}(t)| \leq r_{\theta,i}, \tag{25}$$

   so that effective inward lateral correction is preserved.
3. The relaxation variables $\delta_{x,i}(t)$ and $\delta_{y,i}(t)$ are adjusted according to available maneuvering capability and are driven toward zero when sufficient maneuvering capability is restored.

The resulting design problem is therefore not to force an infeasible deadline boundary under arbitrary saturation, but to preserve executable-boundary feasibility under a temporary capability shortage and to recover the nominal boundary when sufficient maneuvering capability is restored.

3. Methodology

This section proposes a capability-aware executable-boundary recovery controller (CAEBR) to maintain executable-boundary feasibility and promote nominal-boundary recovery. CAEBR consists of three mutually coupled layers, as shown in Figure 2. The fast layer performs real-time executable-boundary regulation, heading-support stabilization, priority-based lateral recovery, and matched residual compensation. The slow layer coordinates the relaxation variables, heading-correction authority, and lateral recovery intensity on a slower timescale according to maneuvering capability and residual-load information. The adaptive residual-information layer provides matched residual estimates and conservative residual-load indicators for compensation and scheduling.

The novelty of CAEBR lies in how these layers are coupled through the executable-boundary variable: the fast layer enforces the currently executable boundary, the slow layer regulates its relaxation and recovery according to capability indicators, and the residual-information layer supplies conservative load information for this scheduling. Therefore, the layered structure is not used as a standalone source of novelty, but as a mechanism for converting online capability information into enforceable transient-performance recovery.

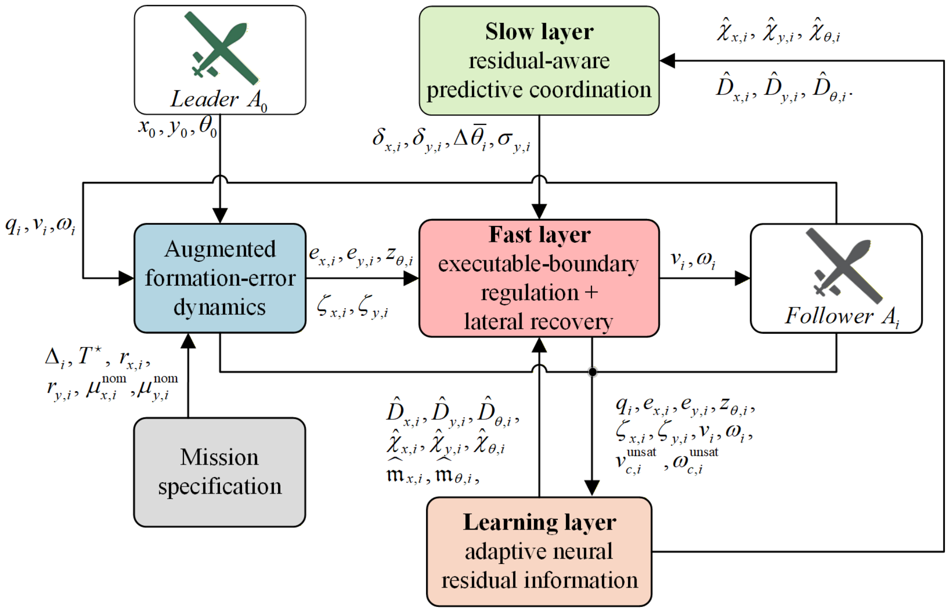

Figure 2. CAEBR control framework.

Before presenting the controller, we specify the admissible coordination variables and feasibility conditions used throughout this section. The executable-boundary relaxation variables and recovery-related scheduling variables $\delta_{x,i}$, $\delta_{y,i}$, $\Delta\bar{\theta}_i$, and $\sigma_{y,i}$ are internal variables generated by the controller. They are implemented through projection, saturation, and rate-limiting operators and hence satisfy, by design,

$$\begin{aligned} 0 \le \delta_{j,i}(t) \le \bar{\delta}_j, \qquad 0 \le \sigma_{y,i}(t) \le \bar{\sigma}_{y,i}, \\ |\Delta\bar{\theta}_i(t)| \le \bar{\theta}_\Delta, \qquad 0 < \bar{\theta}_i(t) = \bar{\theta}_{0,i} + \Delta\bar{\theta}_i(t) \le \bar{\theta}_{\max}, \end{aligned} \tag{26}$$

where $j \in \{x, y\}$. The projection and rate-limiting rules for the executable boundary are selected such that

$$0 < \underline{\mu}_{j,i} \le \mu_{j,i}^{\text{act}}(t) \le \bar{\mu}_{j,i} < 1, \qquad |\dot{\mu}_{j,i}^{\text{act}}(t)| \le \bar{\rho}_{j,i}. \tag{27}$$

The admissibility conditions in Equations (26) and (27) are imposed on the actually applied coordination signals, regardless of whether they are generated by the finite-horizon optimizer or by the fallback rule. Therefore, the slow predictive layer is used as a bounded performance scheduler rather than as the sole source of closed-loop stability. The forward-invariance analysis below relies on admissibility of the applied schedule and on the fast-layer inward conditions, not on an unconditional recursive-feasibility claim for the slow finite-horizon optimization.

Assumption 3. *For each follower i, the matched longitudinal and heading-support equivalent residual dynamics are continuous and bounded on a compact operating domain. Moreover, they can be approximated by bounded neural basis functions with bounded approximation errors. Specifically, there exist unknown ideal constant weights $W_{x,i}^*$ and $W_{\theta,i}^*$ such that*

$$\mathfrak{m}_{x,i} = W_{x,i}^{*\top} \Phi_{x,i}(s_i^{\text{NN}}) + \varepsilon_{x,i}, \qquad |\varepsilon_{x,i}| \le \bar{\varepsilon}_{x,i}, \tag{28}$$

and

$$\mathfrak{m}_{\theta,i} = W_{\theta,i}^{*\top}\Phi_{\theta,i}(s_i^{\mathrm{NN}}) + \varepsilon_{\theta,i}, \qquad |\varepsilon_{\theta,i}| \le \bar{\varepsilon}_{\theta,i}. \tag{29}$$

Here, $\Phi_{x,i}(\cdot)$ and $\Phi_{\theta,i}(\cdot)$ are bounded neural basis vectors, s_i^{NN} is a measurable regressor vector, and $\varepsilon_{x,i}$ and $\varepsilon_{\theta,i}$ are bounded approximation errors. The equivalent residuals $\mathfrak{m}_{x,i}$ and $\mathfrak{m}_{\theta,i}$ denote theoretical matched residual dynamics and are not assumed to be directly measurable.

The adaptive weights are updated with projection operators. Their initial values are selected within the projection sets,

$$\hat{W}_{x,i}(0) \in \Omega_x, \qquad \hat{W}_{\theta,i}(0) \in \Omega_\theta, \tag{30}$$

and the projection radii are chosen sufficiently large so that the ideal weights $W_{x,i}^*$ and $W_{\theta,i}^*$ belong to the corresponding compact analysis sets.

3.1. Unified Fast-Layer Controller for Executable-Boundary Regulation and Lateral Recovery

The fast layer is designed to enforce the executable boundary in real time while promoting nominal-boundary recovery whenever sufficient maneuvering capability is available. It combines executable-boundary regulation, priority-based lateral recovery, and matched residual compensation in a single bounded control structure.

The adaptive residual-information layer supplies the matched residual estimates $\hat{\mathfrak{m}}_{x,i}$ and $\hat{\mathfrak{m}}_{\theta,i}$, as well as the conservative residual-load indicators $\hat{D}_{x,i}$, $\hat{D}_{y,i}$, and $\hat{D}_{\theta,i}$.

The available maneuvering capability is quantified from input margins and residual-load indicators. To avoid algebraic dependence between capability indices and the commands being designed, the input-margin factors are computed from measurable or previously held command-margin indicators. Define

$$v_{\mathrm{mid}} = \frac{v_{\min} + v_{\max}}{2}, \qquad R_v = \frac{v_{\max} - v_{\min}}{2}. \tag{31}$$

The speed-margin factor is

$$s_{v,i} = \mathrm{sat}_{[0,1]}\left(1 - \frac{|v_i - v_{\mathrm{mid}}|}{R_v}\right), \tag{32}$$

and the turn-rate margin factor is

$$s_{\omega,i} = \mathrm{sat}_{[0,1]}\left(\frac{\omega_{\max} - |\omega_i|}{\omega_{\max}}\right). \tag{33}$$

The residual-quality factors are defined as

$$\begin{aligned} s_{d_x,i} &= \mathrm{sat}_{[0,1]}\left(\frac{a_x}{a_x + \hat{D}_{x,i}}\right), \quad s_{d_y,i} = \mathrm{sat}_{[0,1]}\left(\frac{a_y}{a_y + \hat{D}_{y,i}}\right), \\ s_{d_\theta,i} &= \mathrm{sat}_{[0,1]}\left(\frac{a_\theta}{a_\theta + \hat{D}_{\theta,i}}\right). \end{aligned} \tag{34}$$

where $a_x, a_y, a_\theta > 0$ are normalization constants. The estimated capability indices are then given by

$$\begin{aligned} \widehat{\chi}_{x,i} &= s_{v,i} s_{d_x,i}, \\ \widehat{\chi}_{y,i} &= s_{\omega,i} s_{d_\theta,i} s_{d_y,i}, \\ \widehat{\chi}_{\theta,i} &= s_{\omega,i} s_{d_\theta,i}. \end{aligned} \tag{35}$$

Here, $\widehat{\chi}_{x,i}$ characterizes the estimated available longitudinal authority, $\widehat{\chi}_{\theta,i}$ characterizes heading-support authority, and $\widehat{\chi}_{y,i}$ further includes the lateral residual-load indicator because lateral recovery is indirectly achieved through heading-induced coupling. The scheduled gains are chosen as

$$k_{\nu,i}(\widehat{\chi}_{\nu,i}) = k_{\nu,\min} + \big(k_{\nu,\max} - k_{\nu,\min}\big)\widehat{\chi}_{\nu,i}, \qquad \nu \in \{x, y, \theta\}, \tag{36}$$

where $k_{\nu,\max} > k_{\nu,\min} > 0$.

Using the executable boundary, define the normalized transformed errors

$$\check{e}_{x,i} = \frac{\tanh(\kappa_x e_{x,i})}{\mu^{\mathrm{act}}_{x,i}(t)}, \qquad \check{e}_{y,i} = \frac{\tanh(\kappa_y e_{y,i})}{\mu^{\mathrm{act}}_{y,i}(t)}, \tag{37}$$

and the corresponding transformed variables

$$\zeta_{x,i} = \operatorname{artanh}(\check{e}_{x,i}), \qquad \zeta_{y,i} = \operatorname{artanh}(\check{e}_{y,i}). \tag{38}$$

As long as $|\check{e}_{x,i}| < 1$ and $|\check{e}_{y,i}| < 1$, the transformed position errors remain within the executable boundary.

Lemma 1. *Consider follower i under the augmented error dynamics Equation (14). Suppose that, in a compact operating region, the follower maintains positive forward speed, bounded heading-support error, bounded filtering mismatch, and sufficient turn-rate margin. Assume that the virtual-heading command is generated toward the lateral-error-reducing side, i.e.,*

$$\operatorname{sgn}(\theta_{v,i}) = -\operatorname{sgn}(\zeta_{y,i}), \qquad \zeta_{y,i} \neq 0, \tag{39}$$

and assume further that the induced heading-support sector is nondegenerate. Let $c_{y,i}(t)$ denote the instantaneous lateral inward-sector gain induced by the current forward speed, heading-support authority, turn-rate margin, transformation gain, and admissible coordination variables. Suppose that, on the considered operating interval, this gain admits a uniform positive lower bound and the remaining transformed lateral mismatch admits a uniform upper bound, namely

$$c_{y,i}(t) \geq \underline{c}_{y,i} > 0, \qquad \left|\Gamma_{y,i}\Delta^{\mathrm{lat}}_{y,i} + \Pi_{y,i}\right| \leq \bar{\Delta}_{y,i}. \tag{40}$$

Then the lateral transformed-error channel satisfies

$$\zeta_{y,i}\dot{\zeta}_{y,i} \leq -\underline{c}_{y,i}\zeta_{y,i}\tanh(\zeta_{y,i}) + |\zeta_{y,i}|\bar{\Delta}_{y,i}, \tag{41}$$

where $\zeta_{y,i}$ is the transformed lateral error defined in Equation (38).

Proof. From the augmented lateral error dynamics in Equation (14), the lateral transformed-error dynamics can be written on the considered compact operating region as

$$\dot{\zeta}_{y,i} = \Gamma_{y,i}(e_{y,i}, \mu^{\mathrm{act}}_{y,i})\dot{e}_{y,i} + \Pi_{y,i}(e_{y,i}, \mu^{\mathrm{act}}_{y,i}, \dot{\mu}^{\mathrm{act}}_{y,i}), \tag{42}$$

where $\Gamma_{y,i}(\cdot) > 0$ is the positive transformation gain induced by the prescribed-performance mapping, and $\Pi_{y,i}(\cdot)$ collects the boundary-variation term. Since $\mu^{\mathrm{act}}_{y,i}$ is bounded away from zero and one and $|\dot{\mu}^{\mathrm{act}}_{y,i}|$ is bounded, both $\Gamma_{y,i}$ and $\Pi_{y,i}$ are bounded on the compact set.

The lateral error derivative can be decomposed as

$$\dot{e}_{y,i} = \dot{e}^{\mathrm{head}}_{y,i} + \Delta^{\mathrm{lat}}_{y,i}, \tag{43}$$

where $\dot{e}_{y,i}^{\text{head}}$ denotes the component induced by the heading-support direction and forward motion, while $\Delta_{y,i}^{\text{lat}}$ collects leader-induced terms, filtering mismatch, saturation effects, and lateral residual disturbances. Under the inward-sign condition

$$\operatorname{sgn}(\theta_{v,i}) = -\operatorname{sgn}(\zeta_{y,i}), \qquad \zeta_{y,i} \neq 0, \tag{44}$$

the heading-support direction points toward the lateral-error-reducing side. The resulting inward-sector coefficient may vary with the instantaneous forward speed, turn-rate margin, heading-support authority, transformation gain, and slow-layer coordination variables. Under the stated uniform executable-sector margin, there exists a lower bound $\underline{q}_{y,i} > 0$ such that

$$\zeta_{y,i}\Gamma_{y,i}\dot{e}_{y,i}^{\text{head}} \leq -\underline{q}_{y,i}\zeta_{y,i}\tanh(\zeta_{y,i}) \tag{45}$$

on the compact operating region.

Moreover, the remaining terms are bounded. Hence, there exists a constant $\bar{q}_{y,i} > 0$ such that

$$\left|\zeta_{y,i}\left(\Gamma_{y,i}\Delta_{y,i}^{\text{lat}} + \Pi_{y,i}\right)\right| \leq |\zeta_{y,i}|\bar{q}_{y,i}. \tag{46}$$

Combining the preceding two inequalities gives

$$\zeta_{y,i}\dot{\zeta}_{y,i} \leq -\underline{q}_{y,i}\zeta_{y,i}\tanh(\zeta_{y,i}) + |\zeta_{y,i}|\bar{q}_{y,i}. \tag{47}$$

Letting

$$\underline{c}_{y,i} = \underline{q}_{y,i}, \qquad \bar{\Delta}_{y,i} = \bar{q}_{y,i}, \tag{48}$$

yields Equation (41). This completes the proof. □

To quantify the urgency of lateral nominal-boundary recovery, define

$$\xi_{y,i}(t) = \frac{|h_y(e_{y,i}(t))| - \mu_{y,i}^{\text{nom}}(t)}{\max\{1 - \mu_{y,i}^{\text{nom}}(t), \varepsilon_\xi\}}, \qquad \varepsilon_\xi > 0, \tag{49}$$

and

$$\rho_{y,i}(t) = \operatorname{sat}_{[0,1]}\left(\xi_{y,i}(t)\right). \tag{50}$$

When the lateral transformed error remains within the nominal boundary, $\rho_{y,i} = 0$, whereas larger values of $\rho_{y,i}$ indicate stronger urgency for nominal-boundary re-entry.

Turn-rate availability for lateral recovery is evaluated by

$$\gamma_{\omega,i}(t) = \operatorname{sat}_{[0,1]}\left(1 - \frac{|\omega_{m,i}(t)|}{\omega_{\max}}\right), \tag{51}$$

and the heading-support margin factor is

$$\gamma_{\theta,i}(t) = \operatorname{sat}_{[0,1]}\left(1 - \frac{|z_{\theta,i}(t)|}{r_{\theta,i}}\right). \tag{52}$$

The factor $\gamma_{\theta,i}$ suppresses aggressive lateral recovery when the heading-support tube is close to saturation.

Let $\sigma_{y,i}(t) \geq 0$ be the slow recovery-intensity variable generated by the coordination layer. The overall lateral recovery priority is defined as

$$\pi_{y,i}(t) = \operatorname{sat}_{[0,1]}\left(\rho_{y,i}(t) + \kappa_\sigma\sigma_{y,i}(t)\right)\gamma_{\omega,i}(t)\gamma_{\theta,i}(t), \qquad \kappa_\sigma > 0. \tag{53}$$

The available virtual heading-correction authority is

$$\bar{\theta}_i = \bar{\theta}_{0,i} + \Delta\bar{\theta}_i, \qquad 0 < \bar{\theta}_i \leq \bar{\theta}_{\max}. \tag{54}$$

The bounded virtual heading law is designed as

$$\theta_{v,i} = \mathrm{sat}_{[-\bar{\theta}_{\max},\bar{\theta}_{\max}]}\left(-\bar{\theta}_i(1+\alpha_\theta \pi_{y,i})\tanh(k_{y,i}(\widehat{\chi}_{y,i})\zeta_{y,i}) - \beta_\theta \pi_{y,i}\tanh(\zeta_{y,i})\right), \tag{55}$$

where $\alpha_\theta > 0$ and $\beta_\theta > 0$.

The heading-support filter Equation (12) gives

$$\dot{\psi}_i = \frac{\theta_{v,i} - \psi_i}{\tau_\psi}. \tag{56}$$

The speed command is designed as

$$\begin{aligned} v_{c,i}^{\mathrm{unsat}} = {} & v_0\cos(\psi_i - z_{\theta,i}) - \omega_0\Big(\Delta_{x,i}\sin(\psi_i - z_{\theta,i}) + \Delta_{y,i}\cos(\psi_i - z_{\theta,i})\Big) \\ & + \omega_{m,i}e_{y,i} + (1-\alpha_v\pi_{y,i})[k_{x,i}(\widehat{\chi}_{x,i}) + \beta_x]\tanh(\zeta_{x,i}) + \hat{\mathfrak{m}}_{x,i}, \end{aligned} \tag{57}$$

where $0 < \alpha_v < 1$ and $\beta_x > 0$. The term $\omega_{m,i}e_{y,i}$ compensates the measurable longitudinal–lateral coupling in a bounded manner on the executable-boundary domain. The bounded nonlinear feedback $\tanh(\zeta_{x,i})$ is used instead of an unbounded linear transformed-error feedback.

The turn-rate command is designed as

$$\omega_{c,i}^{\mathrm{unsat}} = \omega_0 - \dot{\psi}_i - k_{\theta,i}(\widehat{\chi}_{\theta,i})\tanh(\lambda_\theta z_{\theta,i}) - \beta_z r_{\theta,i}\tanh\!\left(\frac{z_{\theta,i}}{r_{\theta,i}}\right) - \hat{\mathfrak{m}}_{\theta,i}, \qquad \lambda_\theta > 0, \quad \beta_z > 0, \tag{58}$$

where the bounded nonlinear damping term replaces the unbounded linear heading feedback.

The applied inputs are

$$v_i = \mathrm{sat}_{[v_{\min},v_{\max}]}\left(v_{c,i}^{\mathrm{unsat}}\right), \qquad \omega_i = \mathrm{sat}_{[-\omega_{\max},\omega_{\max}]}\left(\omega_{c,i}^{\mathrm{unsat}}\right). \tag{59}$$

Because the feedback terms in Equation (55), (57) and (58) are bounded functions, and because the adaptive weights are confined to compact projection sets, the unsaturated commands are bounded on the admissible executable-boundary domain. In particular, there exists a finite constant $\bar{v}_{c,i} > 0$ such that

$$|v_{c,i}^{\mathrm{unsat}}(t)| \leq \bar{v}_{c,i}. \tag{60}$$

One admissible bound is

$$\bar{v}_{c,i} = \bar{v}_0 + \bar{\omega}_0(|\Delta_{x,i}| + |\Delta_{y,i}|) + \omega_{\max}\bar{e}_{y,i} + k_{x,\max} + \beta_x + \bar{\hat{\mathfrak{m}}}_{x,i}, \tag{61}$$

where

$$\bar{e}_{y,i} = \frac{1}{\kappa_y}\operatorname{artanh}(\bar{\mu}_{y,i}) \tag{62}$$

is induced by the admissible executable-boundary condition $\mu_{y,i}^{\mathrm{act}} \leq \bar{\mu}_{y,i} < 1$, and $\bar{\hat{\mathfrak{m}}}_{x,i}$ is a finite bound induced by the projection set and bounded basis functions.

Therefore, the speed saturation discrepancy

$$\epsilon_{v,i} = v_i - v_{c,i}^{\mathrm{unsat}} \tag{63}$$

is bounded by

$$|\epsilon_{v,i}(t)| \leq \bar{\epsilon}_{v,i}, \qquad \bar{\epsilon}_{v,i} = v_{\max} + \bar{v}_{c,i}. \tag{64}$$

Similarly, the turn-rate command is bounded on the heading-support tube and compact projection domain. Hence the turn-rate saturation discrepancy

$$\epsilon_{\omega,i} = \omega_i - \omega_{c,i}^{\text{unsat}} \tag{65}$$

is bounded whenever the executable heading-support condition is satisfied.

3.2. Residual-Aware Slow Predictive Coordination for Boundary Recovery

The bounded fast layer preserves instantaneous executable-boundary regulation when the boundary is compatible with the available maneuvering authority. However, it does not by itself determine how the executable boundary should evolve over time. This recovery and scheduling problem is handled by a slow residual-aware predictive coordinator. Its role is to regulate the relaxation variables, the heading-correction authority, and the lateral recovery intensity on a slower timescale so that temporary feasibility preservation and subsequent nominal-boundary recovery can be balanced explicitly.

The slow layer uses measured errors, estimated capability indices, and conservative residual-load indicators generated by the adaptive residual-information layer. In this way, it coordinates executable-boundary recovery using implementable residual-burden estimates rather than inaccessible physical disturbances or true equivalent residuals.

The slow layer is implemented periodically with sampling period $T_s > 0$. The state vector is defined as

$$X_i(k) = \begin{bmatrix} e_{x,i}(k) & e_{y,i}(k) & z_{\theta,i}(k) & \delta_{x,i}(k) & \delta_{y,i}(k) & \sigma_{y,i}(k) \end{bmatrix}^\top, \tag{66}$$

and the coordination input is defined as

$$u_{c,i}(k) = \begin{bmatrix} v_{\delta,x,i}(k) & v_{\delta,y,i}(k) & \Delta\bar{\theta}_i(k) \end{bmatrix}^\top. \tag{67}$$

Here, $\Delta\bar{\theta}_i(k)$ is a zero-order-held coordination parameter used to adjust the virtual heading-correction authority in Equation (54).

The scalar projection operator over an interval $[a, b]$ is defined by

$$\text{Proj}_{[a,b]}(s,\nu) = \begin{cases} 0, & s = a,\ \nu < 0, \\ 0, & s = b,\ \nu > 0, \\ \nu, & \text{otherwise}. \end{cases} \tag{68}$$

This operator clips the vector field at the interval boundaries and preserves interval invariance.

The executable-boundary relaxation evolves according to

$$\dot{\delta}_{j,i} = \text{Proj}_{[0,\bar{\delta}_j]}\big(\delta_{j,i}, -\lambda_{\delta,j}\delta_{j,i} + c_{\delta,j}(1 - \widehat{\chi}_{j,i}) + v_{\delta,j,i}\big), \qquad j \in \{x, y\}, \tag{69}$$

where $\lambda_{\delta,j} > 0$ is the natural recovery rate, $c_{\delta,j} > 0$ quantifies the effect of estimated capability deficiency, and $v_{\delta,j,i}$ is the coordination adjustment.

The lateral recovery-intensity state evolves as

$$\dot{\sigma}_{y,i} = \text{Proj}_{[0,\bar{\sigma}_{y,i}]}\big(\sigma_{y,i}, -\lambda_{\sigma,i}\sigma_{y,i} + c_{\sigma 1,i}\rho_{y,i} + c_{\sigma 2,i}(1 - \widehat{\chi}_{y,i})\big), \tag{70}$$

where $\lambda_{\sigma,i} > 0$, $c_{\sigma1,i} > 0$, and $c_{\sigma2,i} > 0$. This dynamic equation avoids impulsive lateral-recovery switching and retains a short memory of recent lateral difficulty and capability shortage.

For prediction, the slow layer uses a reduced-order model rather than the full fast closed-loop dynamics. The slow coordinator is a bounded performance scheduler; high-bandwidth stabilization and executable-boundary invariance are supplied by the fast layer. Using Euler discretization with the sampling period T_s, the reduced-order prediction model is written as

$$\begin{aligned}
e_{x,i}(k+1) &= e_{x,i}(k) + T_s\Big[-F^{\mathrm{red}}_{x,i}(k) + \widehat{R}_{x,i}(k)\Big],\\
e_{y,i}(k+1) &= e_{y,i}(k) + T_s\Big[-F^{\mathrm{red}}_{y,i}(k) + \widehat{R}_{y,i}(k)\Big],\\
z_{\theta,i}(k+1) &= z_{\theta,i}(k) + T_s\Big[-F^{\mathrm{red}}_{\theta,i}(k) + \widehat{R}_{\theta,i}(k)\Big],\\
\delta_{x,i}(k+1) &= \Pi_{[0,\bar{\delta}_x]}\Big(\delta_{x,i}(k) + T_s\big[-\lambda_{\delta,x}\delta_{x,i}(k) + c_{\delta,x}\big(1-\widehat{\chi}_{x,i}(k)\big) + v_{\delta,x,i}(k)\big]\Big),\\
\delta_{y,i}(k+1) &= \Pi_{[0,\bar{\delta}_y]}\Big(\delta_{y,i}(k) + T_s\big[-\lambda_{\delta,y}\delta_{y,i}(k) + c_{\delta,y}\big(1-\widehat{\chi}_{y,i}(k)\big) + v_{\delta,y,i}(k)\big]\Big),\\
\sigma_{y,i}(k+1) &= \Pi_{[0,\bar{\sigma}_{y,i}]}\Big(\sigma_{y,i}(k) + T_s\big[-\lambda_{\sigma,i}\sigma_{y,i}(k) + c_{\sigma1,i}\rho_{y,i}(k) + c_{\sigma2,i}\big(1-\widehat{\chi}_{y,i}(k)\big)\big]\Big).
\end{aligned} \tag{71}$$

Here, $\Pi_{[a,b]}(\cdot)$ denotes the static projection onto $[a,b]$.

The reduced-order stabilizing terms are selected consistently with the bounded fast-layer feedback:

$$F^{\mathrm{red}}_{x,i} = \big[k_{x,i}(\widehat{\chi}_{x,i}) + \beta_x\big]\tanh(\zeta_{x,i}), \tag{72}$$

$$F^{\mathrm{red}}_{\theta,i} = k_{\theta,i}(\widehat{\chi}_{\theta,i})\tanh(\lambda_\theta z_{\theta,i}) + \beta_z r_{\theta,i}\tanh\!\left(\frac{z_{\theta,i}}{r_{\theta,i}}\right), \tag{73}$$

and

$$F^{\mathrm{red}}_{y,i} = \underline{\phi}_{y,i}\tanh(\zeta_{y,i}). \tag{74}$$

The term $F^{\mathrm{red}}_{y,i}$ represents a conservative inward lateral effect induced by the virtual-heading law within the heading-support tube. The quantities $\widehat{R}_{x,i}$, $\widehat{R}_{y,i}$, and $\widehat{R}_{\theta,i}$ are estimated conservative mismatch indicators held constant over the prediction horizon. A typical implementable choice is

$$\widehat{R}_{j,i}(k) = c_{R,j}\hat{D}_{j,i}(k), \qquad c_{R,j} > 0, \qquad j \in \{x,y,\theta\}. \tag{75}$$

The objective function is

$$J_i(k) = J_{r,i}(k) + J_{u,i}(k) + J_{c,i}(k). \tag{76}$$

The recovery component is

$$J_{r,i} = \sum_{p=0}^{N_p-1}\Big[q_{\delta x}\delta^2_{x,i}(p|k) + q_{\delta y}\delta^2_{y,i}(p|k) + q_{ex}e^2_{x,i}(p|k) + q_{ey}e^2_{y,i}(p|k) + q_\theta z^2_{\theta,i}(p|k)\Big]. \tag{77}$$

The lateral-urgency component is

$$J_{u,i} = \sum_{p=0}^{N_p-1}\Big[q_\rho\rho^2_{y,i}(p|k) + q_\sigma\sigma^2_{y,i}(p|k)\Big]. \tag{78}$$

The coordination-conservatism component is

$$J_{c,i} = \sum_{p=0}^{N_c-1} \left[w_{\delta x} v_{\delta,x,i}^2(p|k) + w_{\delta y} v_{\delta,y,i}^2(p|k) + w_\theta \Delta\bar{\theta}_i^2(p|k) \right] + \sum_{p=0}^{N_c-1} \rho_c \widehat{\kappa}_i(k) \left[\left(\frac{|\widehat{v}_{c,i}(p|k)| - \bar{v}_{\text{safe}}}{v_{\text{scale}}} \right)_+^2 + \left(\frac{|\widehat{\omega}_{c,i}(p|k)| - \bar{\omega}_{\text{safe}}}{\omega_{\text{scale}}} \right)_+^2 \right], \tag{79}$$

where $(s)_+ = \max\{s, 0\}$, $\bar{v}_{\text{safe}}$ and $\bar{\omega}_{\text{safe}}$ are safety thresholds, and

$$v_{\text{scale}} := v_{\max} - v_{\min}, \qquad \omega_{\text{scale}} := \omega_{\max}. \tag{80}$$

The predicted command indicators $\widehat{v}_{c,i}$ and $\widehat{\omega}_{c,i}$ are obtained by evaluating the bounded fast-layer command laws Equations (57) and (58) along the reduced-order predicted states, with residual-load indicators frozen at their current values.

The residual-dependent weight is defined as

$$\widehat{\kappa}_i(k) = \kappa_0 + \kappa_{d_x} \hat{D}_{x,i}(k) + \kappa_{d_y} \hat{D}_{y,i}(k) + \kappa_{d_\theta} \hat{D}_{\theta,i}(k), \qquad \kappa_0, \kappa_{d_x}, \kappa_{d_y}, \kappa_{d_\theta} > 0. \tag{81}$$

Thus, command-margin depletion is penalized more strongly when the estimated residual burden is large.

The slow-layer coordination is subject to the executable-boundary constraints

$$|h_x(e_{x,i})| \le \mu_{x,i}^{\text{nom}} + \delta_{x,i}, \qquad |h_y(e_{y,i})| \le \mu_{y,i}^{\text{nom}} + \delta_{y,i}, \tag{82}$$

the relaxation bounds

$$0 \le \delta_{x,i} \le \bar{\delta}_x, \qquad 0 \le \delta_{y,i} \le \bar{\delta}_y, \tag{83}$$

the admissible transformation-domain bound

$$\mu_{j,i}^{\text{nom}} + \delta_{j,i} \le \bar{\mu}_{j,i} < 1, \qquad j \in \{x, y\}, \tag{84}$$

the heading-support tube constraint

$$|z_{\theta,i}| \le r_{\theta,i}, \tag{85}$$

the recovery-intensity constraint

$$0 \le \sigma_{y,i} \le \bar{\sigma}_{y,i}, \tag{86}$$

and the coordination-input constraints

$$|v_{\delta,j,i}| \le \bar{v}_{\delta,j}, \qquad |\Delta\bar{\theta}_i| \le \bar{\theta}_\Delta, \qquad 0 < \bar{\theta}_{0,i} + \Delta\bar{\theta}_i \le \bar{\theta}_{\max}. \tag{87}$$

The slow predictive coordination problem solved at each sampling instant k is

$$\begin{aligned} \min_{\mathcal{U}_i(k)} \quad & J_i(k) \\ \text{s.t.} \quad & \text{prediction model Equation (71)}, \\ & \text{constraints Equations (82)–(87)}, \\ & X_i(0|k) = X_i(k), \end{aligned} \tag{88}$$

where

$$\mathcal{U}_i(k) = \{u_{c,i}(0|k), u_{c,i}(1|k), \dots, u_{c,i}(N_c - 1|k)\} \tag{89}$$

is the coordination-input sequence, N_p is the prediction horizon, $N_c \leq N_p$ is the coordination horizon, and the input is held constant for $p \geq N_c$.

The slow predictive coordinator is used as a bounded performance-scheduling and recovery-coordination mechanism. It is implemented periodically with sampling period $T_s > 0$. Between two consecutive updates, the coordination variables are applied through zero-order hold.

At each update instant, if the optimization problem Equation (88) is feasible, only the first optimized coordination input is applied. The resulting update is followed by projection and saturation operators, so that the admissibility constraints in Equations (26) and (27) are satisfied at all times. If the optimization problem is infeasible or temporarily unavailable, no recursive-feasibility claim is invoked. Instead, the coordinator applies an admissibility-preserving fallback rule: the previously applied admissible coordination values are first held by zero-order hold; if such values are unavailable or violate the rate limits, the recovery inputs are reset to conservative bounded values and then passed through the same projection, saturation, and rate-limiting operators. This fallback may slow nominal-boundary recovery, but it preserves Equations (26) and (27), which are the conditions required by the fast-layer invariance proof.

The recovery of the executable boundary is promoted through the relaxation dynamics Equation (69). Specifically, if the estimated capability is sufficiently high and the recovery action satisfies

$$v_{\delta,j,i}(t) \leq -\bar{c}_{\delta,j} + (\lambda_{\delta,j} - \underline{\lambda}_{\delta,j})\delta_{j,i}(t), \qquad c_{\delta,j}(1 - \widehat{\chi}_{j,i}) \leq \bar{c}_{\delta,j}, \tag{90}$$

with $0 < \underline{\lambda}_{\delta,j} < \lambda_{\delta,j}$, then

$$\dot{\delta}_{j,i}(t) \leq -\underline{\lambda}_{\delta,j}\delta_{j,i}(t) \tag{91}$$

in the projected-vector-field sense. Thus, once sufficient maneuvering capability is restored and recovery-oriented admissible actions are selected, the relaxation variables decay and the executable boundary is recovered toward the nominal boundary.

3.3. Adaptive Neural Residual-Information Layer

The adaptive residual-information layer supports the fast and slow layers by providing implementable residual information. It does not replace the model-based control backbone. Instead, it produces two complementary outputs: adaptive matched residual estimates $\hat{\mathfrak{m}}_{x,i}$ and $\hat{\mathfrak{m}}_{\theta,i}$ for the longitudinal and heading-support channels and conservative residual-load indicators $\hat{D}_{x,i}$, $\hat{D}_{y,i}$, and $\hat{D}_{\theta,i}$ for capability assessment and slow-layer recovery coordination.

For each follower i, let s_i^{NN} collect the measurable tracking errors, heading-support variables, applied inputs, previous command-margin indicators, and boundary-relaxation variables. The equivalent residual quantities are introduced at the analysis level as

$$\mathfrak{m}_{x,i}(t) = \dot{e}_{x,i}(t) - \widehat{\dot{e}}_{x,i}^{\mathrm{nom}}(t), \qquad \mathfrak{m}_{y,i}(t) = \dot{e}_{y,i}(t) - \widehat{\dot{e}}_{y,i}^{\mathrm{nom}}(t), \qquad \mathfrak{m}_{\theta,i}(t) = \dot{z}_{\theta,i}(t) - \widehat{\dot{z}}_{\theta,i}^{\mathrm{nom}}(t), \tag{92}$$

where $\widehat{\dot{e}}_{x,i}^{\mathrm{nom}}$, $\widehat{\dot{e}}_{y,i}^{\mathrm{nom}}$, and $\widehat{\dot{z}}_{\theta,i}^{\mathrm{nom}}$ denote nominal model-based predictions generated from the known fast-layer structure.

For the matched longitudinal and heading-support channels, the adaptive neural approximators are defined as

$$\hat{\mathfrak{m}}_{x,i} = \hat{W}_{x,i}^{\top}\Phi_{x,i}(s_i^{\mathrm{NN}}), \qquad \hat{\mathfrak{m}}_{\theta,i} = \hat{W}_{\theta,i}^{\top}\Phi_{\theta,i}(s_i^{\mathrm{NN}}), \tag{93}$$

where $\Phi_{x,i}(\cdot)$ and $\Phi_{\theta,i}(\cdot)$ are bounded neural basis vectors, and only the output-layer weights $\hat{W}_{x,i}$ and $\hat{W}_{\theta,i}$ are adapted online. This preserves the standard linear-in-the-parameters structure required for Lyapunov-based adaptive analysis.

The parameter estimation errors are defined as

$$\tilde{W}_{x,i} = W^*_{x,i} - \hat{W}_{x,i}, \qquad \tilde{W}_{\theta,i} = W^*_{\theta,i} - \hat{W}_{\theta,i}. \tag{94}$$

For use in the adaptive laws, define the longitudinal transformation gain

$$a_{x,i}(t) := \frac{\kappa_x \operatorname{sech}^2(\kappa_x e_{x,i}(t))}{\mu^{\mathrm{act}}_{x,i}(t)\big(1 - \tilde{e}^2_{x,i}(t)\big)}. \tag{95}$$

The adaptive update directions are defined as

$$\tau_{x,i} = \Gamma_x \Phi_{x,i}(s_i^{\mathrm{NN}}) a_{x,i} \zeta_{x,i} - \sigma_x \Gamma_x \hat{W}_{x,i}, \tag{96}$$

and

$$\tau_{\theta,i} = \Gamma_\theta \Phi_{\theta,i}(s_i^{\mathrm{NN}}) z_{\theta,i} - \sigma_\theta \Gamma_\theta \hat{W}_{\theta,i}. \tag{97}$$

The adaptive laws are

$$\begin{aligned} \dot{\hat{W}}_{x,i} &= \mathrm{Proj}_{\Omega_x}\big(\hat{W}_{x,i}, \tau_{x,i}\big), \\ \dot{\hat{W}}_{\theta,i} &= \mathrm{Proj}_{\Omega_\theta}\big(\hat{W}_{\theta,i}, \tau_{\theta,i}\big), \end{aligned} \tag{98}$$

where $\Gamma_x = \Gamma_x^\top > 0$, $\Gamma_\theta = \Gamma_\theta^\top > 0$, $\sigma_x > 0$, and $\sigma_\theta > 0$. These update laws depend only on measurable regressors, transformed errors, heading-support error, and the current parameter estimates. They do not require direct measurement of $\mathfrak{m}_{x,i}$, $\mathfrak{m}_{\theta,i}$, $\dot{e}_{x,i}$, or $\dot{z}_{\theta,i}$.

For a generic compact projection set of the form

$$\Omega_W = \{\hat{W} \in \mathbb{R}^q : \|\hat{W}\| \le W_{\max}\}, \tag{99}$$

the projection operator is given by

$$\mathrm{Proj}_{\Omega_W}(\hat{W}, \tau) = \begin{cases} \tau, & \|\hat{W}\| < W_{\max}, \\ \tau, & \|\hat{W}\| = W_{\max},\ \hat{W}^\top \tau \le 0, \\ \left(I - \dfrac{\hat{W}\hat{W}^\top}{\|\hat{W}\|^2}\right)\tau, & \|\hat{W}\| = W_{\max},\ \hat{W}^\top \tau > 0. \end{cases} \tag{100}$$

In the actual adaptive laws,

$$\Omega_x = \{\hat{W}_x \in \mathbb{R}^{q_x} : \|\hat{W}_x\| \le W_{x,\max}\}, \qquad \Omega_\theta = \{\hat{W}_\theta \in \mathbb{R}^{q_\theta} : \|\hat{W}_\theta\| \le W_{\theta,\max}\}. \tag{101}$$

The projection operator guarantees that if $\hat{W}(0) \in \Omega_W$, then $\hat{W}(t) \in \Omega_W$ for all $t \ge 0$. Moreover, for $\tilde{W} = W^* - \hat{W}$, it satisfies

$$\tilde{W}^\top \Gamma^{-1}\Big[\mathrm{Proj}_{\Omega_W}(\hat{W}, \tau) - \tau\Big] \le 0. \tag{102}$$

The lateral residual is handled differently. Since $e_{y,i}$ is not directly actuated, no adaptive neural cancellation term is introduced for the lateral channel. Nevertheless, the lateral channel may still contribute to capability degradation. Therefore, the residual-information layer generates a non-compensating lateral residual-load indicator from measurable prediction mismatch. At sampling instants t_ℓ, define

$$\iota_{y,i}(t_\ell) = \left| \frac{e_{y,i}(t_\ell) - e_{y,i}(t_{\ell-1})}{t_\ell - t_{\ell-1}} - \widehat{\dot{e}}^{\mathrm{nom}}_{y,i}(t_{\ell-1}) \right|. \tag{103}$$

The resulting quantity is an implementable finite-difference residual-load indicator, not a direct measurement of the true residual $\mathfrak{m}_{y,i}$.

The residual-load indicators are constructed with explicit saturation:

$$\begin{aligned}\hat{D}_{x,i}(t) &= \mathrm{sat}_{[0,\bar{D}_x]}\left(d_{0,x} + \alpha_{D,x} \max_{\tau\in[t-T_w,t]} |\hat{\mathfrak{m}}_{x,i}(\tau)|\right),\\ \hat{D}_{\theta,i}(t) &= \mathrm{sat}_{[0,\bar{D}_\theta]}\left(d_{0,\theta} + \alpha_{D,\theta} \max_{\tau\in[t-T_w,t]} |\hat{\mathfrak{m}}_{\theta,i}(\tau)|\right),\\ \hat{D}_{y,i}(t) &= \mathrm{sat}_{[0,\bar{D}_y]}\left(d_{0,y} + \alpha_{D,y} \max_{\tau\in[t-T_w,t]} \iota_{y,i}(\tau)\right),\end{aligned} \tag{104}$$

where $T_w > 0$ is the residual-envelope window length, $d_{0,j} > 0$ are baseline robustness margins, $\alpha_{D,j} \geq 1$ are inflation factors, and $\bar{D}_j > 0$ are design upper bounds. The symbol T_w is used for the time window to avoid confusion with the adaptive weight estimates $\hat{W}$. This construction suppresses instantaneous estimation fluctuations, provides conservative residual-load information for capability assessment, and prevents excessively large or noisy residual indicators from destabilizing the scheduling layer.

Let $d^{\mathrm{eq}}_{x,i}(t)$, $d^{\mathrm{eq}}_{y,i}(t)$, and $d^{\mathrm{eq}}_{\theta,i}(t)$ denote the bounded residual terms that remain in the closed-loop error dynamics after applying the nominal feedback and adaptive compensation.

Assumption 4. *The equivalent residual remainders entering the closed-loop analysis are bounded on the admissible operating domain. Specifically, for each follower i, there exist finite positive constants $\bar{d}^{\mathrm{eq}}_{x,i}$, $\bar{d}^{\mathrm{eq}}_{y,i}$, and $\bar{d}^{\mathrm{eq}}_{\theta,i}$ such that*

$$|d^{\mathrm{eq}}_{x,i}(t)| \leq \bar{d}^{\mathrm{eq}}_{x,i}, \qquad |d^{\mathrm{eq}}_{y,i}(t)| \leq \bar{d}^{\mathrm{eq}}_{y,i}, \qquad |d^{\mathrm{eq}}_{\theta,i}(t)| \leq \bar{d}^{\mathrm{eq}}_{\theta,i}. \tag{105}$$

The detailed stability, forward-invariance, boundedness, and conditional-recoverability properties of the proposed CAEBR controller are established in Appendix A.

4. Simulation Studies

In this section, CAEBR is compared with representative baselines selected from the mechanism-level and recent fixed-wing formation-control families identified in the literature review: a prescribed-performance control method (PPC), a prescribed-time prescribed-performance variant (PT-PPC), a disturbance-observer-based robust controller (DOB), a recent finite-time extended-state-observer fixed-wing consensus baseline (FT-ESO), and a model predictive controller (MPC). PPC represents fixed prescribed-boundary enforcement, PT-PPC represents prescribed-time single-envelope enforcement, DOB represents robust residual-compensated tracking, FT-ESO represents a recent fixed-wing finite-time observer/consensus design, and MPC represents optimization-based constrained tracking with soft constraints. PT-PPC and FT-ESO are included in the Scenario 1 nominal-tracking comparison, the Scenario 2 saturated-recovery comparison, and the Scenario 3 6-DoF command-execution comparison. Scenario 2 remains the principal stress test because it directly examines whether a prescribed-time or observer-based fixed-wing formation controller can replace capability-aware executable-boundary recovery under saturation and large initial deviations. These baselines are not claimed to cover every existing fixed-wing formation controller; instead, they provide mechanism-level and recent fixed-wing comparators for evaluating whether CAEBR contributes beyond prescribed-performance tracking, prescribed-time single-envelope tracking, disturbance compensation, finite-time ESO-based consensus tracking, and conventional soft-constrained receding-horizon control.

Within each reported comparison, the included controllers use the same leader–follower geometry, tracking-error definitions, actuator saturation limits, disturbances, and initial conditions. This benchmark selection is intended to balance reviewer-facing breadth with reproducibility. Fully reproducing multiple recent fixed-wing state-of-the-art controllers would require controller-specific fault models, event-triggering or communication protocols, aerodynamic/inner-loop assumptions, and parameter-selection rules that are not identical to the present deadline-boundary executability setting. Therefore, the comparison combines mechanism-level baselines that isolate the competing control ideas with one recent fixed-wing ESO/consensus baseline implemented under the same outer-loop command interface. The resulting benchmark set is used to test whether CAEBR contributes a distinct capability-aware executable-boundary recovery function, rather than to claim exhaustive dominance over all modern fixed-wing formation controllers.

4.1. Compared Control Schemes

4.1.1. PPC Controller

For each channel, the normalized and transformed errors are defined as

$$\xi_{\nu,i} = \frac{e_{\nu,i}}{\rho_{\nu,i}(t)}, \qquad \varepsilon_{\nu,i} = \operatorname{artanh}(\xi_{\nu,i}), \qquad \nu \in \{x, y, \theta\}, \tag{106}$$

where $\rho_{\nu,i}(t)$ denotes a standard exponentially decaying prescribed-performance function. Since the lateral motion of the fixed-wing follower is not directly actuated, the PPC baseline uses a bounded virtual-heading command:

$$\theta_{v,i}^{\mathrm{PPC}} = -\bar{\theta}_i \tanh\left(k_{y,i}^{\mathrm{ppc}} \varepsilon_{y,i}\right). \tag{107}$$

For a fair comparison, the same filtered heading-support structure is adopted:

$$\tau_\psi \dot{\psi}_i^{\mathrm{PPC}} + \psi_i^{\mathrm{PPC}} = \theta_{v,i}^{\mathrm{PPC}}, \qquad z_{\theta,i}^{\mathrm{PPC}} = \psi_i^{\mathrm{PPC}} - \eta_i. \tag{108}$$

The speed and turn-rate commands are selected as

$$v_{c,i}^{\mathrm{PPC}} = v_0 \cos\eta_i - k_{x,i}^{\mathrm{ppc}} \tanh(\varepsilon_{x,i}), \tag{109}$$

and

$$\omega_{c,i}^{\mathrm{PPC}} = \omega_0 - \dot{\psi}_i^{\mathrm{PPC}} - k_{\theta,i}^{\mathrm{ppc}} \tanh(\varepsilon_{\theta,i}). \tag{110}$$

The final applied inputs are saturated by the same actuator limits used for all methods.

4.1.2. Prescribed-Time Prescribed-Performance Controller (PT-PPC)

To strengthen the comparison with a mechanism-close prescribed-time baseline, a simplified prescribed-time prescribed-performance controller is added as an advanced single-envelope baseline. This controller follows the prescribed-time fixed-wing tracking idea in which the user specifies a convergence deadline $T^\star$ and the feedback intensity is increased before that time [26,27]. For implementation consistency with the present kinematic formation model, PT-PPC uses the same normalized transformed errors as PPC, but multiplies the feedback channels by a bounded prescribed-time gain

$$g_T(t) = \begin{cases} \min\left\{1 + \dfrac{a_T (t/T^\star)^2}{\epsilon_T + 1 - t/T^\star}, \bar{g}_T\right\}, & t < T^\star, \\ 1, & t \geq T^\star, \end{cases} \tag{111}$$

where $a_T > 0$, $\epsilon_T > 0$, and $\bar{g}_T > 1$ keep the prescribed-time gain bounded under actuator saturation. The PT-PPC speed, virtual-heading, and turn-rate commands are implemented as

$$v_{c,i}^{\mathrm{PT}} = v_0 \cos \eta_i - k_{x,i}^{\mathrm{PT}} \tanh\left(g_T(t)\varepsilon_{x,i}\right), \tag{112}$$

$$\theta_{v,i}^{\mathrm{PT}} = -\bar{\theta}_i^{\mathrm{PT}} \tanh\left(k_{y,i}^{\mathrm{PT}} g_T(t)\varepsilon_{y,i}\right), \tag{113}$$

and

$$\omega_{c,i}^{\mathrm{PT}} = \omega_0 - \dot{\psi}_i^{\mathrm{PT}} - k_{\theta,i}^{\mathrm{PT}} \tanh\left(\lambda_\theta^{\mathrm{PT}} g_T(t) z_{\theta,i}^{\mathrm{PT}}\right). \tag{114}$$

The final commands are saturated by the same $v_{\min}$, $v_{\max}$, and $\omega_{\max}$ limits as the other controllers. Unlike CAEBR, PT-PPC still enforces a single prescribed envelope and does not generate an online executable boundary or a relaxation-recovery state. It therefore provides a direct test of whether simply strengthening a prescribed-time prescribed-performance envelope can replace capability-aware boundary relaxation in nominal, saturated-recovery, and 6-DoF command-execution cases.

4.1.3. DOB Controller

The lateral channel is handled through a bounded virtual-heading command:

$$\theta_{v,i}^{\mathrm{DOB}} = -\bar{\theta}_i \tanh\left(k_{y,i}^{\mathrm{DOB}} e_{y,i}\right), \tag{115}$$

together with the same filtered heading-support definition:

$$\tau_\psi \dot{\psi}_i^{\mathrm{DOB}} + \psi_i^{\mathrm{DOB}} = \theta_{v,i}^{\mathrm{DOB}}, \qquad z_{\theta,i}^{\mathrm{DOB}} = \psi_i^{\mathrm{DOB}} - \eta_i. \tag{116}$$

The DOB speed and turn-rate commands are given by

$$v_{c,i}^{\mathrm{DOB}} = v_0 \cos \eta_i - k_{x,i}^{\mathrm{DOB}} e_{x,i} - \rho_{x,i}^{\mathrm{DOB}} \tanh\left(\frac{\hat{d}_{x,i}^{\mathrm{eq}}}{d_{x,i}^0}\right), \tag{117}$$

and

$$\omega_{c,i}^{\mathrm{DOB}} = \omega_0 - \dot{\psi}_i^{\mathrm{DOB}} - k_{\theta,i}^{\mathrm{DOB}} z_{\theta,i}^{\mathrm{DOB}} - \rho_{\theta,i}^{\mathrm{DOB}} \tanh\left(\frac{\hat{d}_{\theta,i}^{\mathrm{eq}}}{d_{\theta,i}^0}\right). \tag{118}$$

The final applied inputs are saturated by the same actuator limits used for all methods.

4.1.4. Finite-Time ESO Fixed-Wing Consensus Baseline (FT-ESO)

To benchmark against a recent fixed-wing formation-control design rather than only mechanism-level baselines, an additional finite-time ESO consensus-style baseline is implemented based on the fixed-wing UAV formation controller of Yu et al. [20]. The original method combines a distributed finite-time extended-state observer, event-triggered communication, and composite anti-disturbance consensus control. For implementation consistency with the present leader–follower outer-loop interface, the baseline is adapted as a simplified FT-ESO controller that uses the same relative-error variables, the same speed and turn-rate command limits, and the same filtered heading-support structure as the other baselines. It should therefore be read as an implementation-consistent modern fixed-wing observer/consensus baseline, not as a full reproduction of the event-triggered 3-D controller in [20].

The finite-time observer correction is implemented with $\mathrm{sig}_\alpha(s) = \mathrm{sgn}(s)|s|^\alpha$, where $0 < \alpha < 1$. For the longitudinal and heading-support channels, the observer states satisfy

$$\begin{aligned}
\dot{\hat{e}}_{x,i} &= -k_{x0}\hat{e}_{x,i} + \hat{d}_{x,i} + l_{x1}\,\mathrm{sig}_{\alpha_1}(e_{x,i} - \hat{e}_{x,i}),\\
\dot{\hat{d}}_{x,i} &= l_{x2}\,\mathrm{sig}_{\alpha_2}(e_{x,i} - \hat{e}_{x,i}),\\
\dot{\hat{z}}_{\theta,i} &= -k_{\theta 0}\hat{z}_{\theta,i} + \hat{d}_{\theta,i} + l_{\theta 1}\,\mathrm{sig}_{\alpha_1}(z_{\theta,i} - \hat{z}_{\theta,i}),\\
\dot{\hat{d}}_{\theta,i} &= l_{\theta 2}\,\mathrm{sig}_{\alpha_2}(z_{\theta,i} - \hat{z}_{\theta,i}).
\end{aligned} \tag{119}$$

The resulting speed and turn-rate commands use finite-time sign-power feedback and disturbance compensation,

$$\begin{aligned}
v_{c,i}^{\mathrm{FT}} &= v_0\cos\eta_i - \omega_0(\Delta x_i \sin\eta_i + \Delta y_i\cos\eta_i) + k_{x,i}^{\mathrm{FT}}\,\mathrm{sig}_{\beta_x}(e_{x,i}) + k_{x\ell,i}^{\mathrm{FT}} e_{x,i} + \hat{d}_{x,i},\\
\omega_{c,i}^{\mathrm{FT}} &= \omega_0 - \dot{\psi}_i^{\mathrm{FT}} - k_{\theta,i}^{\mathrm{FT}}\,\mathrm{sig}_{\beta_\theta}(z_{\theta,i}^{\mathrm{FT}}) - k_{\theta\ell,i}^{\mathrm{FT}} z_{\theta,i}^{\mathrm{FT}} - \hat{d}_{\theta,i}.
\end{aligned} \tag{120}$$

The lateral channel is guided by a bounded virtual heading $\theta_{v,i}^{\mathrm{FT}} = -\bar{\theta}_i^{\mathrm{FT}}\tanh(k_{y,i}^{\mathrm{FT}}\,\mathrm{sig}_{\beta_y}(e_{y,i}))$. Unlike CAEBR, FT-ESO does not generate an executable boundary, a relaxation state, or a capability-aware recovery schedule.

4.1.5. MPC Controller

The MPC baseline is implemented as a soft-constrained receding-horizon tracker using the same fixed-wing relative-error kinematics, filtered heading-support variable, and actuator saturation model as the other controllers. For compact notation, the tracking-error components of its local discrete prediction model are written as

$$\mathbf{e}_i(k+1) = A_i\mathbf{e}_i(k) + B_i\mathbf{u}_i(k) + G_i\mathbf{w}_i(k), \tag{121}$$

where

$$\mathbf{e}_i(k) = \begin{bmatrix} e_{x,i}(k)\\ e_{y,i}(k)\\ z_{\theta,i}(k)\end{bmatrix}, \qquad \mathbf{u}_i(k) = \begin{bmatrix} v_{c,i}(k)\\ \omega_{c,i}(k)\end{bmatrix}, \tag{122}$$

and $\mathbf{w}_i(k)$ denotes a bounded leader-motion and disturbance-mismatch term. The matrices A_i and B_i are obtained from the Euler-discretized local prediction model around the current measured state and the previous command, and are updated at every MPC sampling instant. The implementation also propagates the applied-speed and applied-turn-rate actuator states when evaluating input saturation and command-increment limits; Equation (121) only reports the tracking-error components used to define the main state weights. At each sampling instant, the following finite-horizon cost function is minimized:

$$\begin{aligned}
J_i = &\sum_{j=0}^{N_p-1}\Big[\mathbf{e}_i^\top(k+j|k)Q\mathbf{e}_i(k+j|k) + \mathbf{u}_i^\top(k+j|k)R\mathbf{u}_i(k+j|k)\Big]\\
&+ \mathbf{e}_i^\top(k+N_p|k)P\mathbf{e}_i(k+N_p|k) + \lambda_\epsilon\sum_{j=0}^{N_p-1}\|\epsilon_i(k+j|k)\|_1,
\end{aligned} \tag{123}$$

where Q, R, and P are diagonal positive definite weighting matrices, and ϵ_i denotes the nonnegative soft-constraint violation vector for $e_{x,i}$, $e_{y,i}$, and $z_{\theta,i}$. The terminal weight P is used as a diagonal terminal penalty selected together with the stage weights; it is not used as an unreported terminal-set certificate, and no recursive-feasibility guarantee is claimed for this baseline MPC. The optimization is subject to the same input bounds used by CAEBR,

$$v_{\min} \le v_{c,i}(k+j|k) \le v_{\max}, \qquad -\omega_{\max} \le \omega_{c,i}(k+j|k) \le \omega_{\max}, \tag{124}$$

as well as input-increment constraints and soft constraints on $e_{x,i}$, $e_{y,i}$, and $z_{\theta,i}$. In all simulations, the MPC sampling period is $T_{\text{MPC}} = 0.10$ s, the prediction horizon and control horizon are $N_p = 12$ and $N_c = 4$, respectively, and the last optimized command is held constant in the prediction for $j \ge N_c$. The first optimized input is applied according to the receding-horizon principle:

$$\begin{bmatrix} v_{c,i}^{\text{MPC}}(k) \\ \omega_{c,i}^{\text{MPC}}(k) \end{bmatrix} = \mathbf{u}_i^{\star}(k|k). \tag{125}$$

4.2. Simulation Setup and Evaluation Metrics

A leader–follower formation consisting of one leader and three followers is considered. The leader is initialized as

$$(x_0(0), y_0(0), \theta_0(0)) = (0, 0, 0). \tag{126}$$

The desired formation offsets in the leader body frame are selected as

$$p_{d,1} = (-25, -20)\ \text{m}, \qquad p_{d,2} = (-25, 20)\ \text{m}, \qquad p_{d,3} = (-50, 0)\ \text{m}. \tag{127}$$

For a fair comparison, the controllers included in each scenario are evaluated using the same formation offsets, leader trajectory, input saturation limits, disturbance profiles, and initial conditions. The control inputs are subject to the same speed and turn-rate constraints for all methods included in that scenario. The baseline parameters are tuned once for each scenario and then kept fixed over the full trajectory, without time-segment-dependent retuning. The common comparison metrics are the tracking RMSE, nominal-boundary violation ratio, final nominal re-entry time, heading-support RMSE, and heading-tube violation ratio. The executable-boundary exceedance metric is reported separately because only CAEBR generates the online executable boundary $\mu_{j,i}^{\text{act}}$; the baseline controllers are therefore compared against the same nominal deadline boundary and heading-support tube within their corresponding scenarios.

To make the parameter selection reproducible, the following tuning protocol is used. For each scenario, the deadline parameters, actuator limits, leader trajectory, disturbance profile, and initial conditions are fixed before controller tuning. For CAEBR, the relaxation budgets, recovery rates, and heading-authority limits are first selected to satisfy initial executable-boundary feasibility and the actuator-compatible inward conditions used in the analysis; the feedback gains are then increased within the saturation margins until nominal tracking improves without persistent input saturation. For the included PPC, PT-PPC, DOB, FT-ESO, and MPC baselines, the gains or weights are tuned over the same scenario to obtain stable nondivergent tracking, reduce tracking RMSE and nominal-boundary violation, and avoid excessive input chattering. After this one-time scenario-level tuning, no controller is retuned according to time segments or intermediate trajectory observations. Therefore, differences in numerical parameters reflect the different controller structures and design variables rather than different test conditions.

For CAEBR, the most sensitive recovery parameters are the relaxation budgets $\bar{\delta}_j$ and the recovery rates $\lambda_{\delta,j}$. The budgets are selected before feedback-gain tuning, because they determine whether the executable boundary can be initialized and kept inside the admissible transformed-error domain. A practical lower bound is

$$\bar{\delta}_j \geq \max_i \Big[|h_j(e_{j,i}(0))| - \mu_{j,i}^{\text{nom}}(0) \Big]_+ + \varepsilon_j, \qquad j \in \{x, y\}, \tag{128}$$

with a small design margin $\varepsilon_j > 0$, while the upper bound must keep $\mu_{j,i}^{\text{nom}}(t) + \bar{\delta}_j$ below one with margin. Increasing $\bar{\delta}_j$ improves executable-boundary feasibility during severe saturation or large initial errors, but it can increase the recorded nominal-boundary violation and delay final nominal re-entry. Decreasing $\bar{\delta}_j$ gives a tighter mission-level response, but may make the initial or transient executable boundary infeasible.

After the relaxation budget is fixed, $\lambda_{\delta,j}$ is selected according to the desired nominal-boundary recovery time. From the conditional recovery estimate in the analysis, a target decay from $\delta_j(t_r)$ to a small tolerance $\delta_{j,\text{tol}}$ over $T_{\text{rec},j}$ suggests

$$\lambda_{\delta,j} \gtrsim \frac{1}{T_{\text{rec},j}} \ln \frac{\delta_j(t_r)}{\delta_{j,\text{tol}}}, \tag{129}$$

subject to the actuator-compatible inward conditions and the rate limits of the slow coordinator. A larger $\lambda_{\delta,j}$ accelerates recovery toward the nominal boundary when sufficient maneuvering capability returns, whereas an excessively large value can force aggressive re-entry commands and increase input saturation. The normalization constants a_x, a_y, a_θ are chosen near the expected residual-load scale: smaller values make the capability indices more conservative, while larger values make the recovery schedule less sensitive to residual estimates. The fast-layer gains $k_{\nu,\min}$ and $k_{\nu,\max}$, the heading-priority parameters $\alpha_\theta, \beta_\theta, \kappa_\sigma$, and the heading-authority limit $\bar{\theta}_{\max}$ are then increased only within the available speed, turn-rate, bank-angle, and load-factor margins. The projection radii $W_{x,\max}$ and $W_{\theta,\max}$ are selected large enough to contain the expected residual-model weights but finite enough to prevent estimator drift, and the horizons N_p, N_c are chosen as the shortest horizons that still cover the dominant recovery transient without exceeding the available onboard computation time. These sensitivity trends were used to select the reported implementation values; therefore, the selected values represent a conservative feasible tuning rather than an offline optimal parameter set.

The deadline-oriented parameters used in Scenario 1 are listed in Table 1. Scenario 2 uses a saturated-recovery setting with modified boundary and heading-tube parameters, which are stated in the corresponding scenario description.

Table 1. Deadline-oriented simulation parameters for Scenario 1.

Parameter	Value	Description
$T^\star$	20 s	Desired deadline
$r_{x,i}$	1.0 m	Terminal longitudinal error bound
$r_{y,i}$	0.8 m	Terminal lateral error bound
$r_{\theta,i}$	0.12 rad	Heading-support tube radius
κ_x	0.22	Longitudinal transformation parameter
κ_y	0.25	Lateral transformation parameter
$\mu_{x,i}^0$	0.80	Initial longitudinal boundary
$\mu_{y,i}^0$	0.78	Initial lateral boundary
ℓ_x	2	Longitudinal boundary shaping parameter
ℓ_y	2	Lateral boundary shaping parameter
T_f	90 s	Simulation horizon

The following metrics are used for quantitative evaluation.

The averaged longitudinal and lateral tracking errors are evaluated by

$$\overline{\mathrm{RMSE}}_x = \frac{1}{N_f}\sum_{i=1}^{N_f}\sqrt{\frac{1}{T}\int_0^T e_{x,i}^2(t)\,dt}, \qquad \overline{\mathrm{RMSE}}_y = \frac{1}{N_f}\sum_{i=1}^{N_f}\sqrt{\frac{1}{T}\int_0^T e_{y,i}^2(t)\,dt}. \tag{130}$$

The averaged nominal-boundary violation is defined as

$$\bar{\Gamma}_{\mathrm{nom},j} = \frac{1}{N_f}\sum_{i=1}^{N_f}\frac{1}{T}\int_0^T \frac{\left[|h_j(e_{j,i}(t))| - \mu_{j,i}^{\mathrm{nom}}(t)\right]_+}{1-\mu_{j,i}^{\mathrm{nom}}(t)}\,dt, \qquad j\in\{x,y\}, \tag{131}$$

where $[s]_+ = \max\{s,0\}$.

The CAEBR-specific executable-boundary exceedance metric is defined as

$$\overline{\mathrm{BV}}_{j,i}^{\mathrm{exec}} = \frac{1}{T_f}\int_0^{T_f}\left(|h_j(e_{j,i}(t))| - \mu_{j,i}^{\mathrm{act}}(t)\right)_+ dt, \qquad j\in\{x,y\}. \tag{132}$$

Since $\mu_{j,i}^{\mathrm{act}}$ is generated only by CAEBR, $\overline{\mathrm{BV}}_{j,i}^{\mathrm{exec}}$ is used as a CAEBR-specific executable-feasibility certificate rather than as a common metric imposed on all baselines. The common boundary-related metric for all controllers is the nominal-boundary violation ratio in Equation (131).

The averaged final re-entry time is used to evaluate how quickly the tracking error re-enters the nominal deadline boundary after a temporary violation:

$$\bar{t}_{\mathrm{re},j} = \frac{1}{N_f}\sum_{i=1}^{N_f}\inf\Big\{\tau\in[0,T] : |h_j(e_{j,i}(t))| \le \mu_{j,i}^{\mathrm{nom}}(t),\ \forall t\in[\tau,T]\Big\}, \qquad j\in\{x,y\}. \tag{133}$$

In capability-limited scenarios, $\bar{\Gamma}_{\mathrm{nom},j}$ and $\bar{t}_{\mathrm{re},j}$ describe recovery with respect to the mission-level nominal boundary, whereas $\overline{\mathrm{BV}}_{j,i}^{\mathrm{exec}}$ measures whether the boundary actually enforced by CAEBR is violated. Therefore, these metrics should be interpreted jointly: a conservative executable-boundary relaxation may increase nominal-boundary violation or delay final nominal re-entry while still preserving the enforceable boundary.

For the heading-support channel, the averaged heading-support RMSE is defined as

$$\overline{\mathrm{RMSE}}_\theta = \frac{1}{N_f}\sum_{i=1}^{N_f}\sqrt{\frac{1}{T}\int_0^T z_{\theta,i}^2(t)\,dt}. \tag{134}$$

The heading-support tube violation ratio is defined as

$$\Gamma_{\theta_i} = \frac{1}{T_f}\int_0^{T_f}\mathbf{1}(|z_{\theta,i}(t)| > r_{\theta,i})\,dt. \tag{135}$$

The main controller settings of CAEBR and of the implemented baselines are summarized in Table 2. The values in the table are the implementation settings used in the comparative simulations. They should not be interpreted as unique solutions of the sufficient theoretical inequalities. The theoretical conditions specify admissible ranges and compatibility relations for executable-boundary invariance, heading-support boundedness, and conditional recovery, whereas the reported numerical gains and weights are one admissible implementation selected according to the tuning protocol above.

Table 2. Main controller settings.

Method	Core Gains/Weights	Coordination or Guidance Settings
CAEBR	$k_x : [1.90, 6.95]$, $k_y : [0.70, 1.52]$ $k_\theta : [1.25, 2.30]$	$T_s = 0.20$, $N_p/N_c = 12/4$ $\bar{\theta}_{\max} = 0.389$, $\bar{\delta}_x/\bar{\delta}_y = 0.108/0.55$
PPC	$k_x = 2.43$, $k_y = 0.87$ $k_\theta = 1.59$	$\bar{\theta} = 0.22$ $\tau_\psi = 0.35$
PT-PPC	$k_x = 2.40$, $k_y = 0.88$ $k_\theta = 1.80$	$a_T/\bar{g}_T/\epsilon_T = 0.75/2.30/0.26$ $\bar{\theta} = 0.235$, $\tau_\psi = 0.34$
DOB	$k_x = 1.41$, $k_y = 0.43$ $k_\theta = 2.46$	$l_x = 6.21/9.36$, $l_\theta = 6.26/15.57$ $\bar{\theta} = 0.25$, $\tau_\psi = 0.38$
FT-ESO	$k_x = 1.28$, $k_y = 0.40$ $k_\theta = 2.15$	$l_x = 7.60/15.00$, $l_\theta = 7.80/17.50$ $\bar{\theta} = 0.235$, $\tau_\psi = 0.36$
MPC	$q_x/q_y/q_\theta = 2.69/2.10/5.39$ $r_v/r_\omega = 0.11/0.58$	$N_p/N_c = 12/4$ $\Delta v_{\max}/\Delta\omega_{\max} = 0.72/0.08$

4.3. Scenario 1: Nominal Formation Tracking Under Sufficient Capability

Scenario 1 is designed to examine the nominal tracking behavior of the proposed CAEBR controller when the formation task is feasible and sufficient maneuvering capability is available. In this case, the prescribed nominal performance boundary can be enforced without activating substantial executable-boundary relaxation. Therefore, this scenario is not intended to create a failure case for the baseline controllers. Instead, it evaluates whether CAEBR can preserve nominal tracking accuracy, avoid unnecessary conservatism, and maintain smooth formation evolution under mild disturbances and adequate input authority.

The leader follows a smooth low-curvature S-turn:

$$\begin{aligned} v_0(t) &= 18\ \mathrm{m/s}, \\ \theta_0(t) &= 0.18\sin(0.055t) + 0.07\sin(0.13t). \end{aligned} \tag{136}$$

The followers are initialized with small deviations:

$$\begin{aligned} (x_1, y_1, \theta_1) &= (-28, -20, 0.04), \\ (x_2, y_2, \theta_2) &= (-23, 15, -0.03), \\ (x_3, y_3, \theta_3) &= (-52, 3, 0.02). \end{aligned} \tag{137}$$

Weak time-varying disturbances are applied:

$$\begin{aligned} d_{x,i} &= 0.25\sin(0.12t + \phi_i), \\ d_{y,i} &= 0.20\cos(0.10t + \bar{\phi}_i), \\ d_{\theta,i} &= 0.015\sin(0.18t + \tilde{\phi}_i), \end{aligned} \tag{138}$$

where ϕ_i, $\bar{\phi}_i$, and $\tilde{\phi}_i$ are fixed follower-dependent phases. The same phase values are used for all compared controllers.

The input constraints are

$$v \in [10, 30], \qquad |\omega| \leq 0.42. \tag{139}$$

Figure 3 shows that all six controllers included in Scenario 1 successfully complete the nominal formation-tracking task. Because the leader maneuver is smooth, the initial offsets are small, and the actuator margins are sufficient, no controller exhibits loss of formation or trajectory divergence. The added PT-PPC and FT-ESO baselines also produce bounded nominal-case trajectories, indicating that the prescribed-time single-envelope design and the observer/consensus-style design both remain feasible in this capability-sufficient setting. The formation paths generated by CAEBR remain smooth and well organized throughout the maneuver, without visible oscillatory deformation or excessive transient spreading. Therefore, the proposed capability-aware structure does not degrade the nominal tracking behavior when executable-boundary relaxation is not strongly required.

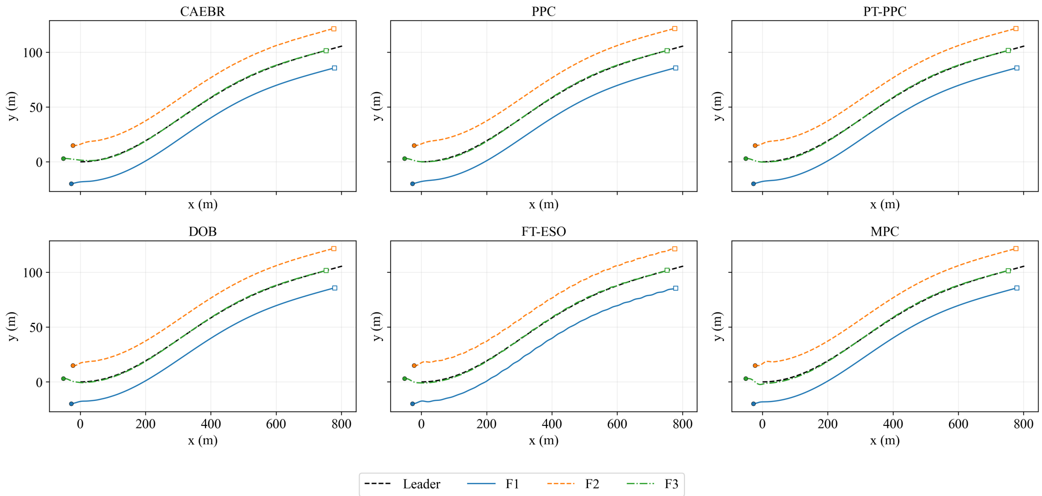

Figure 3. Formation trajectories in Scenario 1.

The representative responses in Figure 4 provide a more detailed comparison. In the longitudinal transformed-error channel, PPC and DOB exhibit larger transient fluctuations, while MPC, FT-ESO, and CAEBR regulate the transformed error rapidly. PT-PPC follows the PPC-type response with a stronger prescribed-time feedback action and remains stable without introducing boundary violation. CAEBR yields a smooth decay profile and maintains a small residual level during the later stage of the maneuver. In the lateral transformed-error channel, PPC produces a larger transient excursion, DOB shows noticeable oscillatory behavior, and PT-PPC reduces the lateral error relative to PPC. FT-ESO further improves the nominal lateral response relative to PPC and PT-PPC, but it introduces a more oscillatory heading-support response than CAEBR. CAEBR keeps the lateral transformed error close to zero for most of the simulation horizon and retains a smoother heading-support response. The heading-support error remains bounded for all methods in this nominal case.

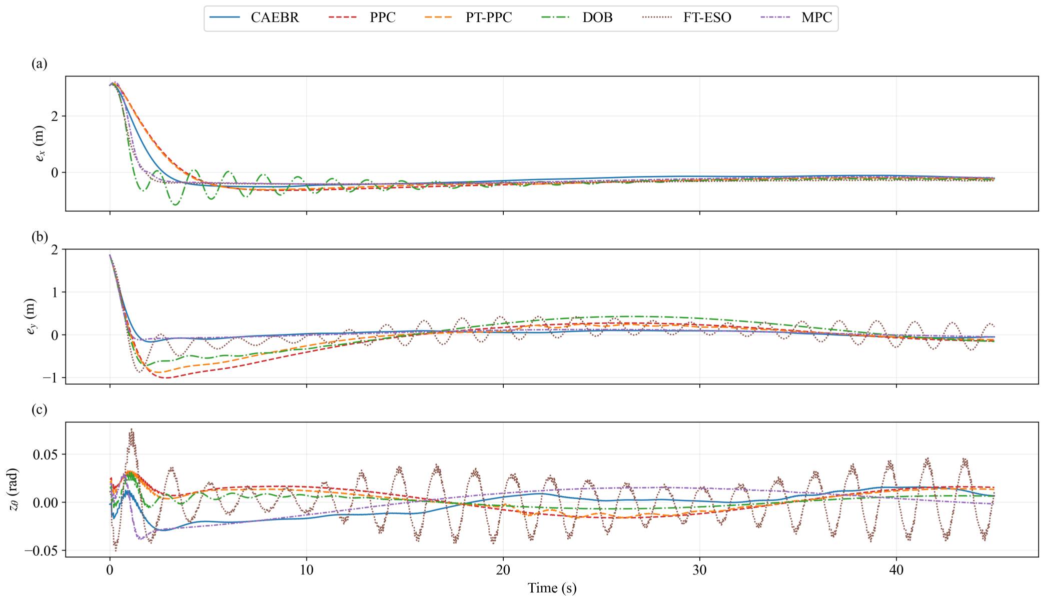

Figure 4. Error responses in Scenario 1. Panels (**a**–**c**) show the representative longitudinal tracking error, lateral tracking error, and heading-support error, respectively.

Table 3 further confirms the nominal tracking performance. CAEBR achieves the smallest lateral RMSE for Followers 1 and 2, with RMSE_y values of 0.189 and 0.398, respectively, while FT-ESO gives the smallest lateral RMSE for Follower 3 with a value of 0.511. This is significant because the lateral channel is indirectly regulated through heading adjustment and forward motion in fixed-wing formation tracking. PPC gives the largest lateral errors for all followers, while DOB and PT-PPC improve the transient response but remain less accurate than CAEBR or FT-ESO in this nominal case. The added FT-ESO baseline provides a stronger observer-based comparison than DOB and obtains competitive nominal tracking, but it still does not include executable-boundary relaxation or recovery scheduling. MPC also remains a strong baseline in this scenario.

Table 3. Quantitative results for Scenario 1.

Follower	Method	RMSE_x	RMSE_y	Γ_x^{nom}	Γ_y^{nom}
1	CAEBR	0.552	0.189	0	0
	PPC	0.668	0.409	0	0
	PT-PPC	0.652	0.344	0	0
	DOB	0.559	0.362	0	0
	FT-ESO	0.524	0.288	0	0
	MPC	0.533	0.191	0	0
2	CAEBR	0.434	0.398	0	0
	PPC	0.582	0.529	0	0
	PT-PPC	0.567	0.495	0	0
	DOB	0.439	0.472	0	0
	FT-ESO	0.416	0.472	0	0
	MPC	0.411	0.489	0	0
3	CAEBR	0.378	0.523	0	0
	PPC	0.479	0.695	0	0
	PT-PPC	0.483	0.632	0	0
	DOB	0.467	0.572	0	0
	FT-ESO	0.422	0.511	0	0
	MPC	0.391	0.558	0	0

In the longitudinal direction, CAEBR remains competitive but is not uniformly the best. For the first two followers, MPC and FT-ESO obtain slightly lower longitudinal RMSE values than CAEBR, whereas for the third follower, CAEBR achieves the smallest longitudinal RMSE. These results show that CAEBR does not sacrifice nominal longitudinal accuracy for robustness-oriented scheduling. Instead, it maintains competitive longitudinal tracking while improving the more challenging lateral regulation for the first two followers and preserving zero nominal-boundary violation.

For all methods and all followers, both Γ_x^{nom} and Γ_y^{nom} are zero. This confirms that the nominal performance boundary is feasible throughout Scenario 1. Therefore, the main distinction among the controllers in this capability-sufficient case lies in tracking accuracy and response smoothness rather than boundary violation.

4.4. Scenario 2: Large Initial Deviation and Saturated Recovery

Scenario 2 is designed to evaluate the capability-aware recovery property of CAEBR under large initial deviations, aggressive leader maneuvers, actuator saturation, and moderate disturbances. In this case, the nominal deadline boundary may become temporarily too demanding for the available fixed-wing maneuvering authority. The purpose of this scenario is therefore to examine whether CAEBR activates the executable-boundary channel during capability-limited intervals, how much nominal-boundary recovery can be obtained after authority becomes available, and whether residual executable-boundary exceedance remains when the selected relaxation budget is conservative.

A piecewise aggressive leader maneuver is used:

$$\begin{aligned}
&v_0 = 18.2, \qquad \omega_0 = 0, \qquad 0 \le t < 10 \text{ s},\\
&v_0 = 18.0, \qquad \omega_0 = 0.28, \qquad 10 \le t < 18 \text{ s},\\
&v_0 = 17.4, \qquad \omega_0 = -0.30, \qquad 18 \le t < 28 \text{ s},\\
&v_0 = 18.2, \qquad \omega_0 = 0.24, \qquad 28 \le t < 40 \text{ s},\\
&v_0 = 17.8, \qquad \omega_0 = -0.22, \qquad 40 \le t < 54 \text{ s},\\
&v_0 = 18.6, \qquad \omega_0 = 0.10, \qquad 54 \le t < 66 \text{ s},\\
&v_0 = 18.8, \qquad \omega_0 = 0, \qquad 66 \le t \le 90 \text{ s}.
\end{aligned} \tag{140}$$

The followers are initialized with large deviations:

$$\begin{aligned}
(x_1, y_1, \theta_1) &= (-18, -42, 0.45),\\
(x_2, y_2, \theta_2) &= (-12, 36, -0.42),\\
(x_3, y_3, \theta_3) &= (-32, 18, 0.36).
\end{aligned} \tag{141}$$

Disturbances are applied:

$$\begin{aligned}
d_{x,i} &= 0.16\sin(0.10t + \phi_i) + 0.08\sin(0.65t + \bar{\phi}_i),\\
d_{y,i} &= 1.15\cos(0.08t + \bar{\phi}_i) + 0.42\sin(0.78t + \phi_i),\\
d_{\theta,i} &= 0.036\sin(0.24t + \tilde{\phi}_i) + 0.014\sin(1.15t).
\end{aligned} \tag{142}$$

The same follower-dependent phase values are used for all compared controllers.

The input constraints are tightened to

$$v \in [16, 22], \qquad |\omega| \le 0.30. \tag{143}$$

For this saturated-recovery scenario, the nominal-boundary and heading-tube parameters are set to

$$r_x = 1.10\ \text{m}, \quad r_y = 1.35\ \text{m}, \quad r_\theta = 0.16\ \text{rad},$$
$$\kappa_x = 0.10, \quad \kappa_y = 0.18, \quad \mu_x^0 = \mu_y^0 = 0.92,$$
$$\ell_x = 1.7, \quad \ell_y = 2.6.$$

Figure 5 shows the formation trajectories under the capability-limited maneuver. Compared with Scenario 1, the large initial deviations, tighter input constraints, and repeated leader turns generate a significantly more demanding recovery process. PPC, PT-PPC, and DOB can track the leader trajectory, but their follower paths exhibit larger transient spreading. PT-PPC slightly improves the path response relative to the ordinary PPC baseline, but it still operates as a single prescribed-time envelope without capability-aware relaxation. The added FT-ESO baseline provides a modern observer/consensus comparison in the same saturated-recovery setting; it improves the longitudinal RMSE relative to CAEBR but does not generate an executable boundary. MPC improves path regularity and reduces the longitudinal tracking error more effectively than CAEBR in this setting. CAEBR still produces a bounded recovery response and keeps the formation from diverging, but the trajectory comparison should be interpreted as evidence of capability-aware recovery rather than uniform trajectory optimality.

The quantitative results in Table 4 show a directional rather than uniform advantage. CAEBR gives $\overline{\text{RMSE}}_x = 12.67$ and $\overline{\text{RMSE}}_y = 8.97$. Relative to PPC, the longitudinal and lateral RMSE values are reduced by approximately 23.67% and 6.06%, respectively. Relative to the added PT-PPC baseline, the corresponding reductions are 20.37% and 4.22%. In the lateral channel, CAEBR also reduces the RMSE relative to DOB, FT-ESO, and MPC by approximately 9.28%, 16.18%, and 28.21%, respectively. However, its longitudinal RMSE is larger than those of DOB, FT-ESO, and MPC. The results therefore support the benefit of capability-aware lateral recovery in this saturated scenario, but they do not indicate that CAEBR is uniformly superior to all baselines in all tracking directions.

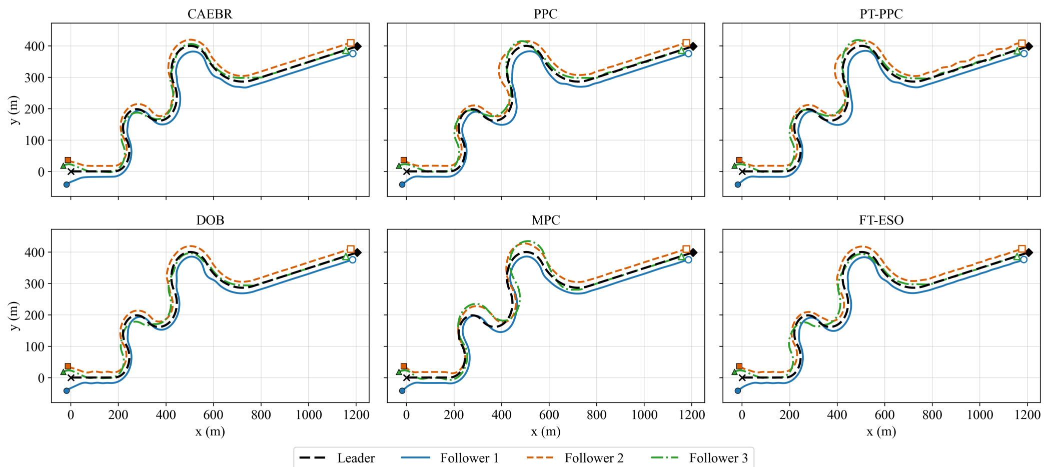

Figure 5. Formation trajectories in Scenario 2. Distinct line styles are used together with color coding to improve black-and-white readability.

Table 4. Quantitative results for Scenario 2.

Method	Tracking Error		Nominal-Boundary Violation		Executable-Boundary Exceedance		Final Re-Entry Time		Heading Tube	
	$\overline{\mathrm{RMSE}}_x$	$\overline{\mathrm{RMSE}}_y$	$\bar{\Gamma}_{\mathrm{nom},x}$	$\bar{\Gamma}_{\mathrm{nom},y}$	$\max_i \overline{\mathrm{BV}}^{\mathrm{exec}}_{x,i}$	$\max_i \overline{\mathrm{BV}}^{\mathrm{exec}}_{y,i}$	$\bar{t}_{\mathrm{re},x}$	$\bar{t}_{\mathrm{re},y}$	$\overline{\mathrm{RMSE}}_\theta$	$\max_i \Gamma_{\theta,i}$
PPC	16.59	9.55	0.51	0.67	-	-	42.26	53.07	0.12	0.23
PT-PPC	15.91	9.37	0.50	0.72	-	-	41.63	45.08	0.13	0.26
DOB	10.59	9.89	0.46	0.63	-	-	40.77	47.24	0.11	0.13
FT-ESO	11.73	10.71	0.49	0.65	-	-	40.65	50.28	0.09	0.09
MPC	7.10	12.50	0.48	0.54	-	-	42.55	46.71	0.45	0.66
CAEBR	12.67	8.97	0.52	0.64	0.37	0.35	38.38	35.55	0.07	0.005

Figures 6 and 7 further illustrate the mechanism behind this improvement. In Figure 6, the relaxation variables δ_x and δ_y increase during the high-demand recovery intervals, especially around and after the deadline $T^\star = 20$ s; their formation-wise maxima reach approximately 0.108 and 0.541, respectively, while remaining below their selected admissible budgets $\bar{\delta}_x = 0.108$ and $\bar{\delta}_y = 0.55$. The larger lateral relaxation is expected in this saturated fixed-wing case because the lateral channel is indirectly regulated through heading and forward motion, whereas the longitudinal relaxation is kept close to its smaller saturation-compatible budget. This behavior indicates that CAEBR activates the executable-boundary channel instead of forcing the nominal boundary when the prescribed transient requirement temporarily exceeds the available maneuvering capability. The resulting executable boundary expands visibly above the nominal boundary during capability-limited intervals. In Figure 7, the dash-dot curves are computed from the same relaxation variables according to $\mu^{\mathrm{act}}_{j,i} = \mu^{\mathrm{nom}}_j + \delta_{j,i}$. Therefore, the vertical difference between the executable and nominal boundaries in each follower panel is consistent with the corresponding δ_x or δ_y curve in the relaxation plot and diagnostic panel. Around the deadline, for example, the lateral executable-boundary gap remains below the selected budget $\bar{\delta}_y = 0.55$, which is consistent with the maximum δ_y value of approximately 0.541. In the final straight-flight segment, the lateral transformed errors decay and remain inside the enlarged executable boundary after approximately 70 s, which removes the late-stage lateral exceedance observed in the previous tuning. The relaxation is still interpreted as a finite mitigation-and-recovery budget rather than as an unconditional feasibility envelope for all early severe transients.

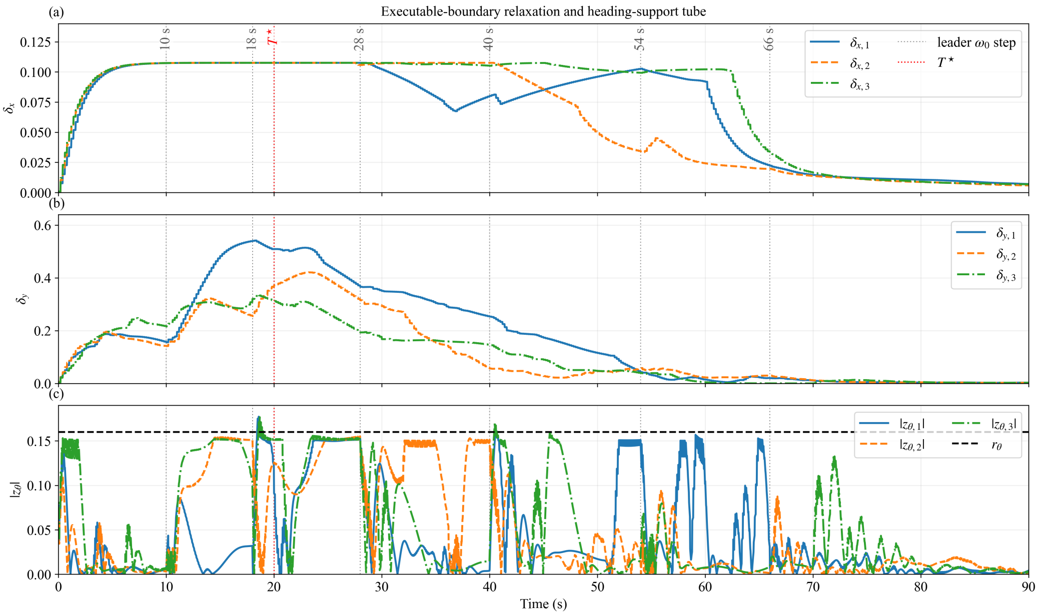

Figure 6. Relaxation and heading-support responses under CAEBR. Panels (**a**–**c**) show the longitudinal relaxation, lateral relaxation, and heading-support tube responses, respectively. The relaxation variables increase visibly during capability-limited intervals and decay as the executable boundary recovers. Gray dotted vertical lines mark the leader turn-rate step times in Scenario 2, and the red dotted line marks the prescribed deadline $T^\star$.

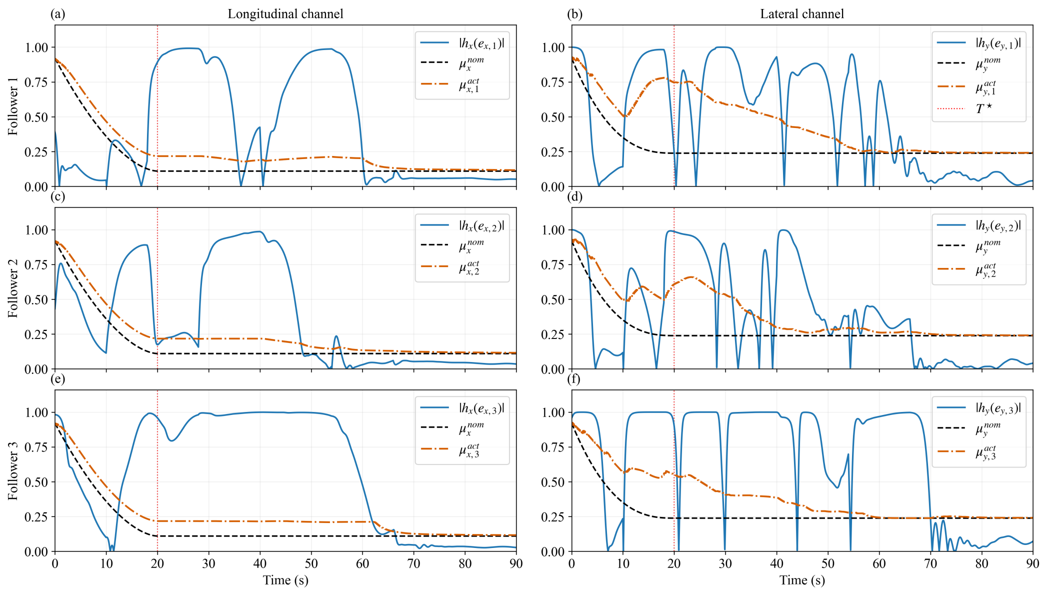

Figure 7. Boundary-tracking results under CAEBR. Panels (**a**–**f**) are arranged by follower and channel, with the longitudinal channel in the left column and the lateral channel in the right column. Solid curves denote transformed-error magnitudes, dashed curves denote nominal deadline boundaries, and dash-dot curves denote executable-boundary levels computed from the nominal boundary plus the corresponding relaxation variable, $\mu_{j,i}^{\mathrm{act}} = \mu_j^{\mathrm{nom}} + \delta_{j,i}$. Hence, the vertical gap between each dash-dot curve and its dashed nominal boundary is the corresponding relaxation variable shown in the relaxation and diagnostic plots; the longitudinal and lateral columns use separate y-axis ranges to improve readability.

Figure 8 provides the corresponding internal diagnostic signals. The formation-wise capability indices decrease during the aggressive-turn and high-recovery-demand intervals, indicating reduced available speed or heading authority and increased residual burden. At the same time, the adaptive residual estimates and residual-load indicators remain bounded and vary with the maneuver demand, so the slow layer receives online information about the current disturbance and compensation burden. The recovery scheduling variables δ_x, δ_y, and $\Delta\bar{\theta}$ are activated during these capability-limited intervals and remain bounded throughout the simulation. The bounded but visibly activated amplitudes of δ_x and δ_y show that the selected relaxation budget provides a moderate capability-aware mitigation channel while still enforcing recovery toward the nominal boundary. These trends show that the boundary relaxation and heading-authority adjustment are triggered by the capability and residual information internally generated by CAEBR, rather than by an externally prescribed time schedule.

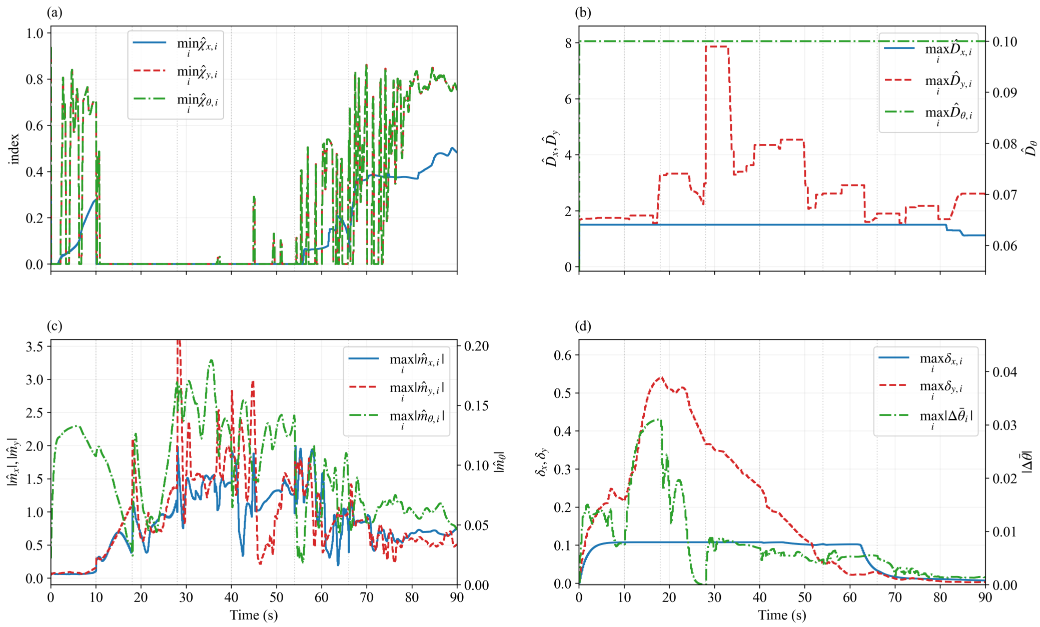

Figure 8. Internal capability and residual diagnostics under CAEBR in Scenario 2. Panels (**a**–**d**) show the capability indices, residual-load indicators, adaptive residual estimates, and recovery scheduling variables, respectively. The capability indices are plotted as formation-wise minima over the three followers, while the residual-load indicators, adaptive residual estimates, and recovery scheduling variables are plotted as formation-wise maxima. Panel (**d**) reports the relaxation variables that define the gap between the nominal and executable boundaries in the boundary-tracking figure.

Figure 7 shows that the executable boundary mitigates the capability gap but does not fully eliminate boundary exceedance in this severe setting. The transformed-error magnitudes are not fully contained during the early and middle high-demand intervals, but the enlarged executable boundary contains the lateral response in the final straight-flight segment. This is reflected in Table 4, where CAEBR gives

$$\max_i \overline{\mathrm{BV}}_{x,i}^{\mathrm{exec}} = 0.37, \max_i \overline{\mathrm{BV}}_{y,i}^{\mathrm{exec}} = 0.35.$$

Therefore, although the nominal deadline boundary is temporarily too restrictive, the selected relaxation budget should be interpreted as a mitigating mechanism rather than a complete executable-feasibility certificate for this severe case. The baseline controllers, including PT-PPC and FT-ESO, do not generate capability-aware executable boundaries; therefore, the executable-boundary exceedance metric is reported only for CAEBR.

This comparison provides an internal interpretation of the executable-boundary mechanism using the same CAEBR trajectory. If the response were judged only against the nominal deadline boundary, the run would have nonzero nominal-boundary violation, with $\overline{\Gamma}_{\mathrm{nom},x} = 0.52$ and $\overline{\Gamma}_{\mathrm{nom},y} = 0.64$. The executable-boundary channel partially reduces the mismatch by temporarily enlarging the enforceable boundary when capability is limited, but the nonzero executable-boundary exceedance shows that the available relaxation budget is still not sufficient to cover all transient demands. Conversely, a fixed permanently enlarged boundary could reduce boundary exceedance only by abandoning recovery toward the nominal deadline requirement. The bounded evolution of δ_x and δ_y in Figure 6, together with the finite final re-entry times in Table 4, shows that CAEBR performs capability-dependent relaxation and recovery rather than fixed relaxation. This distinguishes CAEBR from nominal-only prescribed-boundary tracking, prescribed-time single-envelope tracking, and conventional soft-constrained MPC in which the relaxation variable is not used as an explicit closed-loop capability-recovery signal.

The nominal-boundary violation indices further clarify the recovery behavior. Since the nominal deadline boundary is temporarily infeasible in Scenario 2, all controllers exhibit nonzero nominal-boundary violation. CAEBR obtains

$$\overline{\Gamma}_{\mathrm{nom},x} = 0.52, \overline{\Gamma}_{\mathrm{nom},y} = 0.64.$$

These values are comparable to or larger than those of the baselines because CAEBR explicitly records the intervals in which the nominal boundary is relaxed into an executable boundary. Thus, the nominal-boundary violation ratio should be interpreted together with the executable-boundary metric and the tracking RMSE rather than as an isolated performance index in this capability-limited case. In terms of final re-entry, CAEBR gives

$$\bar{t}_{\mathrm{re},x} = 38.38\ \mathrm{s}, \bar{t}_{\mathrm{re},y} = 35.55\ \mathrm{s}.$$

These re-entry times remain shorter than those of the baselines, indicating that the bounded relaxation-and-recovery channel is compatible with nominal-boundary re-entry after severe transients. This benefit is accompanied by nonzero executable-boundary exceedance and by a longitudinal RMSE that remains worse than those of DOB and MPC.

The heading-support results in Figure 6 and Table 4 show that the lateral recovery action is not achieved by violating the heading-support tube. Under CAEBR, the heading-support error remains below the tube radius throughout the simulation, giving

$$\overline{\mathrm{RMSE}}_{\theta} = 0.07, \max_{i} \Gamma_{\theta,i} = 0.005.$$

By contrast, PPC, PT-PPC, DOB, FT-ESO, and MPC yield larger heading-support errors and larger tube violation ratios. These results indicate that the priority-based lateral recovery mechanism coordinates lateral correction with the available heading margin, while the heading-support margin suppresses excessive heading correction near the tube boundary.

Overall, Scenario 2 demonstrates the main capability–performance coordination property of CAEBR under a severe capability-limited maneuver. When the nominal deadline boundary is temporarily beyond the available maneuvering capability, CAEBR activates a bounded executable-boundary relaxation and improves lateral tracking relative to all five baselines listed in Table 4. The retuned relaxation budget also removes the late straight-flight lateral exceedance in Figure 7, so the remaining executable-boundary exceedance is concentrated in the earlier high-demand recovery interval. However, the visible relaxation amplitudes are still insufficient to fully cover all severe transients; therefore, the scenario should be read as evidence for capability-aware coordination under a finite recovery budget, not as proof that the selected executable boundary fully contains all severe transients. At the same time, the nonzero executable-boundary exceedance and the weaker longitudinal RMSE relative to DOB, FT-ESO, and MPC show that the present tuning does not provide uniform dominance under this severe saturated-recovery case. These results support the usefulness of executable-boundary regulation and relaxation-recovery coordination for deadline-guided fixed-wing UAV formation tracking, while also identifying the need for careful relaxation-budget selection, task-level deadline adjustment, or further controller refinement when complete executable-boundary satisfaction is required.

4.5. Ablation and Complexity Analysis in Scenario 2

To examine whether the proposed architecture is only a collection of redundant components, an ablation study was conducted in Scenario 2, which is the principal capability-limited stress test. All variants used the same leader trajectory, initial deviations, disturbance signals, actuator limits, nominal deadline boundary, and simulation horizon as the full CAEBR run. The tested variants are: the full CAEBR controller; CAEBR without the adaptive residual estimator, where only fixed conservative disturbance bounds are used; CAEBR without the slow predictive coordination layer, where $\delta_x = \delta_y = \Delta\bar{\theta} = 0$ and $\mu_j^{\mathrm{act}} = \mu_j^{\mathrm{nom}}$; and CAEBR without the priority lateral recovery action, where the lateral recovery and safety heading-correction terms in the fast layer are disabled.

Table 5 and Figure 9 show that the three main components have complementary roles rather than only increasing controller complexity. The full-controller RMSE values are computed from the same Scenario 2 run as the CAEBR row in Table 4 and therefore match after rounding; the executable-boundary columns in Table 5 use formation-averaged mean values for ablation comparison, whereas Table 4 reports worst-follower maximum metrics for cross-method comparison. Removing the slow predictive coordination layer eliminates the online executable-boundary relaxation and increases the formation-averaged lateral executable-boundary violation from 0.073 to 0.329, while the maximum relaxation amplitudes become zero. Removing the priority lateral recovery action mainly degrades the lateral channel, increasing $\overline{\mathrm{RMSE}}_y$ from 8.974 to 9.792 and increasing the mean $\mathrm{BV}_y^{\mathrm{exec}}$ from 0.073 to 0.098. Removing the adaptive residual estimator produces a smaller but still visible loss of lateral robustness, increasing $\overline{\mathrm{RMSE}}_y$ from 8.974 to 9.385 and increasing the mean $\mathrm{BV}_y^{\mathrm{exec}}$ from 0.073 to 0.083. The longitudinal RMSE of the residual-estimator ablation is slightly lower than that of the full controller, so the ablation does not support a claim of uniform improvement in every channel; instead, it indicates that the adaptive residual-information layer mainly contributes to lateral robustness in this saturated recovery case.

Table 5. Ablation results in Scenario 2 under the same capability-limited setting. The columns labelled mean executable-boundary violation report formation-averaged temporal mean values. The full-controller row uses the same Scenario 2 run as the CAEBR row in Table 4; Table 4 reports worst-follower maximum executable-boundary metrics, so the two BV columns are not numerically interchangeable.

Variant	$\overline{\mathrm{RMSE}}_x$	$\overline{\mathrm{RMSE}}_y$	Mean $\mathrm{BV}_x^{\mathrm{exec}}$	Mean $\mathrm{BV}_y^{\mathrm{exec}}$	$\bar{\Gamma}_\theta$	max δ_x	max δ_y
Full CAEBR	12.667	8.974	0.245	0.073	0.00296	0.108	0.541
w/o adaptive residual estimator	12.614	9.385	0.245	0.083	0.00304	0.108	0.540
w/o slow predictive coordination	13.098	8.960	0.322	0.329	0.00230	0.000	0.000
w/o priority lateral recovery	12.664	9.792	0.251	0.098	0.00341	0.108	0.542

From a complexity viewpoint, the fast layer is algebraic at each outer-loop control update and only evaluates bounded transformed-error feedback, capability indices, and residual-compensation terms for each follower. The adaptive residual-information layer uses a fixed-size estimator and projection-limited residual envelopes, so its online cost is bounded and independent of the simulation horizon after the estimator size is chosen. The slow predictive coordination layer is the most expensive component because it is executed at the slower period $T_s = 0.20$ s and updates the relaxation and heading-authority variables, but the ablation table and diagnostic figure show that this layer is also the component most directly responsible for reducing executable-boundary violation. Therefore, the full CAEBR architecture is more complex than the ablated variants, but the added complexity is tied to identifiable functions: residual-load awareness, executable-boundary relaxation and recovery, and priority lateral correction under heading and saturation limits.

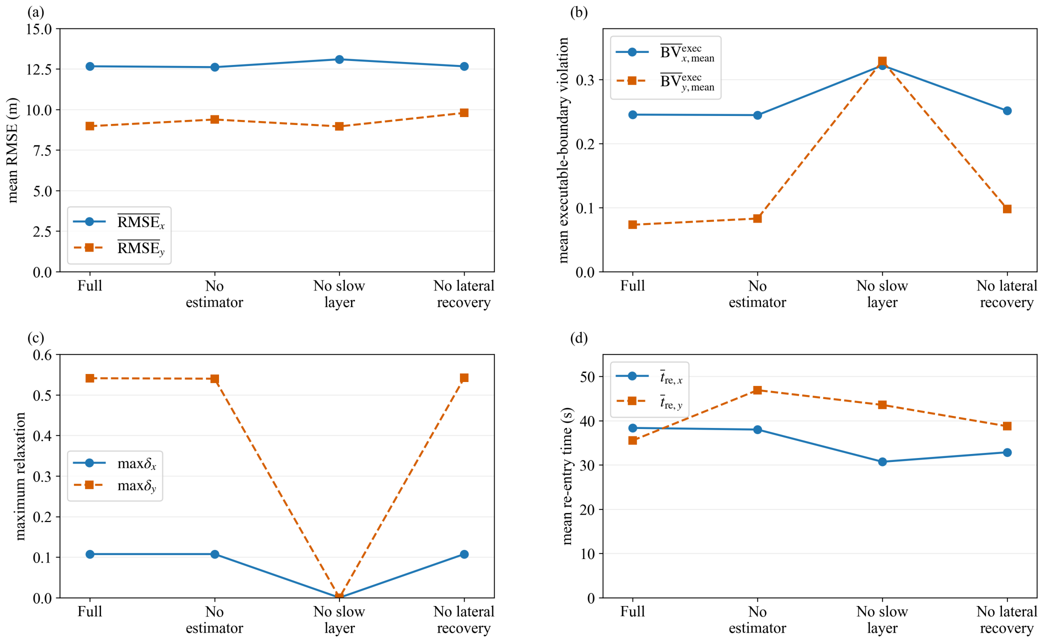

Figure 9. Diagnostic comparison of the Scenario 2 ablation variants. Panels show (**a**) mean RMSE, (**b**) formation-averaged mean executable-boundary violation, (**c**) maximum relaxation amplitude, and (**d**) mean re-entry time under the same capability-limited setting as Table 5.

4.6. Scenario 3: Aerosonde-Class 6-DoF Engineering Validation

To further examine whether the outer-loop speed and turn-rate commands can be executed by a higher-fidelity fixed-wing dynamic plant, Scenario 3 introduces an Aerosonde-class six-degree-of-freedom engineering validation. The validation uses a 12-state rigid-body fixed-wing plant with representative physical, aerodynamic, and propulsion parameters. A common command-to-surface interface maps the outer-loop speed and turn-rate commands to throttle, aileron, elevator, and rudder inputs. The same 6-DoF plant and the same inner command interface are used for CAEBR, PPC, PT-PPC, DOB, FT-ESO, and MPC.

This scenario is designed as a moderately aggressive engineering coupling check. Compared with the preliminary MPC-friendly check, the initial formation offsets and leader excitation are increased so that the 6-DoF plant is evaluated under more demanding command-execution conditions while still allowing all six methods to complete the run. The simulation horizon is set to 80 s, the outer-loop update period is 0.10 s, the commanded speed is constrained by $v \in [23, 27]$ m/s, and the commanded turn rate is constrained by $|\omega| \leq 0.08$ rad/s. The leader uses a 0.6 m/s speed modulation and piecewise turn-rate commands of 0.025, -0.025, and 0.018 rad/s.

Figure 10 shows that all six controllers can be coupled to the Aerosonde-class 6-DoF plant without trajectory divergence under the strengthened command envelope. Figure 11 adds compact summary diagnostics for tracking error, boundary and heading-tube violation, surface-deflection usage, command range, throttle range, and the MPC solver-success rate. Table 6 further reports the corresponding tracking, boundary, actuator, and solver metrics. In this stronger 6-DoF setting, CAEBR, PPC, PT-PPC, and DOB complete the full simulation with zero nominal-boundary and executable-boundary violation. CAEBR reduces the average longitudinal and lateral RMSE relative to PPC from 3.519/5.057 m to

2.906/4.540 m, respectively. Relative to PT-PPC, CAEBR changes the corresponding values from 3.404/4.696 m to 2.906/4.540 m, showing a modest improvement while retaining the same zero-violation result. The FT-ESO baseline obtains lower longitudinal and lateral RMSE than CAEBR in this 6-DoF setting, but it reaches the imposed surface-deflection and speed-command limits and exhibits nonzero lateral nominal-boundary violation of 0.070. MPC also completes the run with a solver success rate of 0.990, but it reaches the imposed surface-deflection and command limits and shows nonzero nominal-boundary, executable-boundary, and heading-tube violation.

The results should be interpreted conservatively. DOB obtains the lowest average RMSE in this strengthened 6-DoF setting, but it uses the full speed-command range and a larger throttle range than CAEBR. FT-ESO also provides a strong observer-based comparison: it improves RMSE relative to CAEBR but does so with full command-range use, surface-limit contact, and nonzero lateral boundary violation, whereas CAEBR keeps zero nominal and executable-boundary violation with a smaller command range. The added PT-PPC baseline behaves similarly to PPC in command-execution load and remains stable, but it still relies on a single prescribed-time envelope rather than an executable-boundary recovery mechanism. MPC remains executable but behaves as a high-activity baseline: its mean turn-rate command is much larger than that of CAEBR, PPC, PT-PPC, DOB, and FT-ESO, and its boundary and heading-support tube violations are summarized in Figure 11. The summary diagnostics also show that FT-ESO and MPC operate closest to the imposed surface-deflection and speed-command limits. Therefore, Scenario 3 is used to support 6-DoF command-execution consistency of the outer-loop formation controllers under a more demanding command envelope, rather than to claim uniform performance dominance or flight-test-level validation.

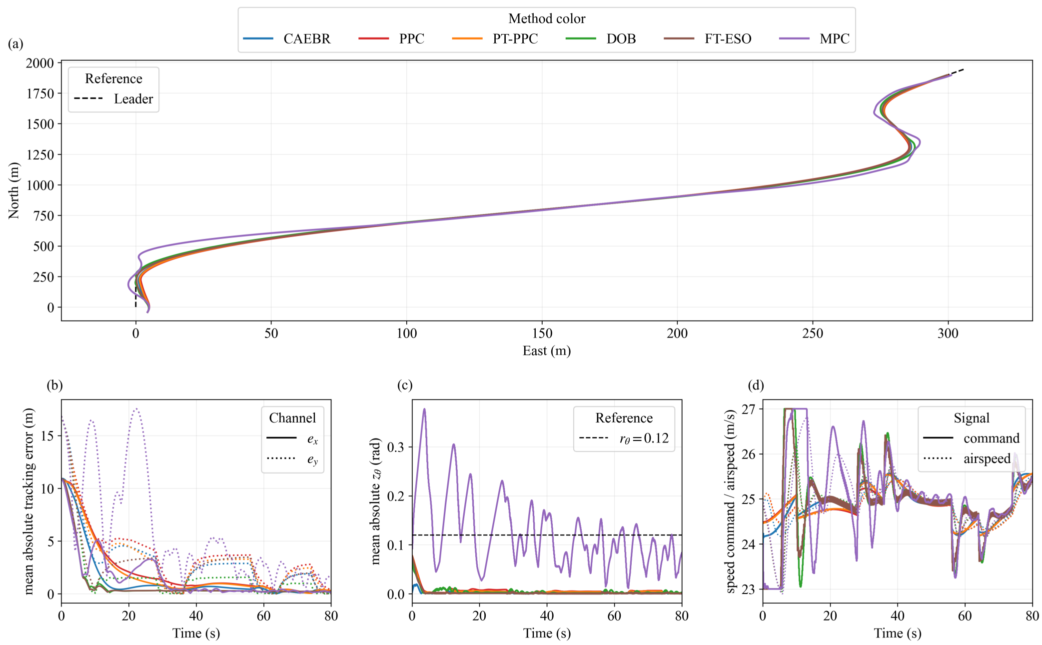

Figure 10. Aerosonde-class 6-DoF engineering validation in Scenario 3. The shared legend above panel (**a**) assigns colors to the six methods, while local inset legends identify the leader reference in panel (**a**), the e_x/e_y channels in panel (**b**), the r_θ reference limit in panel (**c**), and the command/airspeed signals in panel (**d**). The panels show formation-centroid trajectories, mean absolute tracking errors, mean absolute heading-support errors, and representative speed-command tracking errors for CAEBR, PPC, PT-PPC, DOB, FT-ESO, and MPC under the same 6-DoF plant and command-to-surface interface.

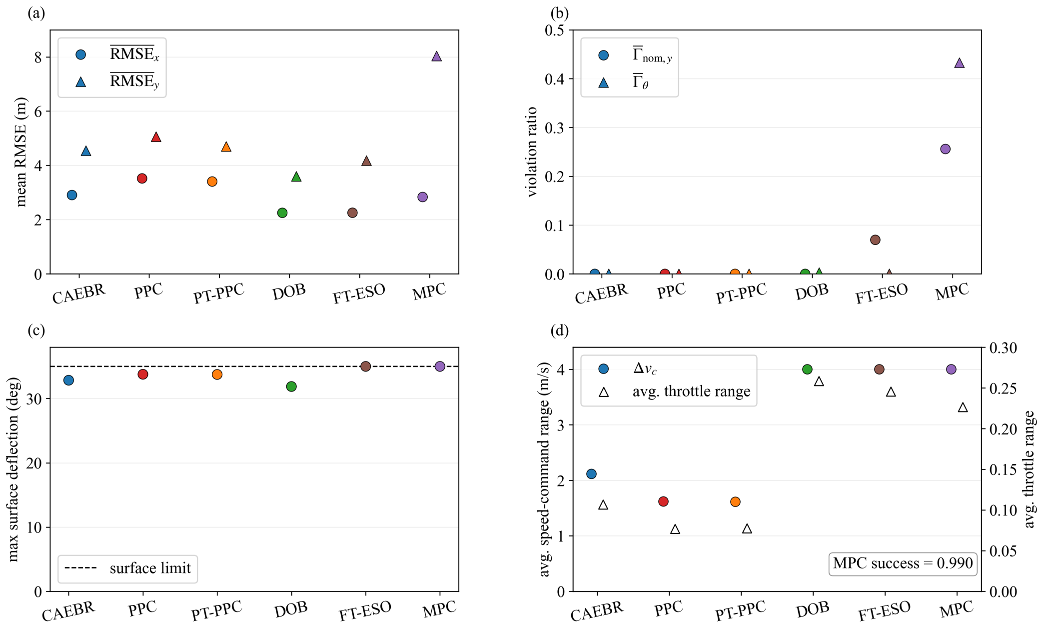

Figure 11. Summary diagnostics for the Aerosonde-class 6-DoF validation in Scenario 3. Panels (**a**–**d**) report mean tracking errors, boundary/heading violation ratios, maximum surface deflection, and command-execution load, respectively.

Table 6. Quantitative results for the Aerosonde-class 6-DoF engineering validation in Scenario 3.

Method	$\overline{\mathrm{RMSE}}_x$	$\overline{\mathrm{RMSE}}_y$	$\overline{\Gamma}_{\mathrm{nom},x/y}$	$\overline{\Gamma}_{\mathrm{act},x/y}$	$\overline{\Gamma}_\theta$	$\delta_{\max}$ (deg)	Δv_c (m/s)	MPC Success
CAEBR	2.906	4.540	0/0	0/0	0	32.845	2.115	–
PPC	3.519	5.057	0/0	0/0	0	33.774	1.618	–
PT-PPC	3.404	4.696	0/0	0/0	0	33.745	1.612	–
DOB	2.250	3.593	0/0	0/0	0.002	31.870	4.000	–
FT-ESO	2.253	4.173	0/0.070	0/0.070	0	35.000	4.000	–
MPC	2.833	8.030	0.022/0.256	0.022/0.256	0.432	35.000	4.000	0.990

5. Practical Implementation and Limitations

The simulations above validate the proposed control-layer mechanism under bounded time-varying disturbances, input saturation, large initial deviations, aggressive leader maneuvers, and the representative Aerosonde-class 6-DoF plant coupling considered in Scenario 3. The disturbance signals in Scenarios 1 and 2 are designed to stress the executable-boundary recovery mechanism and the indirect lateral regulation channel, while Scenario 3 checks whether the resulting outer-loop commands can be executed through a fixed-wing rigid-body dynamic plant and a common command-to-surface interface. These results should not be interpreted as complete atmospheric, hardware-in-the-loop, flight-test, or hardware-timing validation. The present study does not include Dryden or von Karman turbulence models, a validated model of the authors' own airframe, high-fidelity actuator and sensor dynamics, communication delays, hardware-in-the-loop tests, measured onboard computation timing, or outdoor flight experiments. Therefore, the reported results should be understood as simulation-based evidence for executable-boundary feasibility, conditional nominal-boundary recovery, representative 6-DoF command-execution consistency, and comparative tracking behavior.

The executable boundary should therefore be understood as a control-layer approximation of the enforceable transient-performance envelope. It is not claimed to be an exact physical flight envelope obtained by solving a full 6-DoF reachable-set, aerodynamic-stall, load-factor, actuator-rate, and wind-disturbance feasibility problem. A rigorous aircraft-specific derivation would require validated aerodynamic coefficients, actuator dynamics and rate limits, inner-loop bandwidth, atmospheric uncertainty, and reachability or optimal-control analysis. In the present work, these physical limits enter indirectly through the speed and turn-rate saturation, coordinated-turn interpretation, residual-load indicators, and 6-DoF command-execution check; therefore, the reported executable-boundary results should be interpreted as control-layer feasibility evidence rather than a certified physical maneuvering envelope.

From an implementation viewpoint, CAEBR assumes that a lower-level fixed-wing autopilot tracks speed and turn-rate commands with sufficient bandwidth while enforcing the specified saturation limits. The turn-rate limit used by the outer-loop controller should be computed from the admissible coordinated-turn envelope, including bank-angle and load-factor constraints, rather than selected independently of the aircraft. If the inner loop is slower or the admissible bank/load-factor envelope is tighter, the fast-layer gains and the heading-authority bound $\bar{\theta}_{\max}$ should be reduced, or the executable-boundary relaxation budget should be enlarged, so that the actuator-compatible inward conditions used in the analysis remain valid. The fast layer is algebraic at each control step, except for the low-dimensional adaptive residual update with projection. The slow layer is executed at a lower rate and solves a reduced-order coordination problem for the relaxation variables, heading-authority adjustment, and lateral recovery intensity. In the simulations, the slow coordination period is $T_s = 0.20$ s, and the prediction and coordination horizons are $N_p = 12$ and $N_c = 4$, respectively. If the slow optimization is infeasible or temporarily unavailable, the admissibility-preserving fallback rule keeps the applied coordination variables within their prescribed bounds, although nominal-boundary recovery may become slower.

These observations indicate that the proposed method is suitable for implementation as an outer-loop formation-recovery module above an existing fixed-wing autopilot, provided that state estimation, command tracking bandwidth, wind/residual bounds, and onboard optimization time are verified for the target platform. Future work will extend the validation to stochastic wind models, target-airframe 6-DoF identification, measured onboard timing/profiling, hardware-in-the-loop experiments, and flight tests, and will further investigate distributed recovery coordination under communication constraints.

6. Conclusions

This paper studied deadline-guided formation tracking for fixed-wing UAVs under nonholonomic coupling, input saturation, and time-varying uncertainties. The main challenge is the mismatch between the nominal deadline boundary required by the mission layer and the boundary that can be enforced with the available maneuvering capability.

To address this problem, the CAEBR controller was proposed. CAEBR separates the nominal deadline boundary from an executable boundary and coordinates the gap between them online. The controller consists of a bounded fast layer for executable-boundary regulation and lateral recovery, a slow residual-aware predictive coordination layer for boundary relaxation and recovery scheduling, and an adaptive residual-information layer for residual estimation and capability indication.

The theoretical analysis established forward invariance of the executable boundary and heading-support tube, boundedness of closed-loop signals, and conditional recovery of the nominal boundary under the stated admissibility conditions. The simulations showed that CAEBR preserves nominal tracking performance when sufficient maneuvering capability is available and, under large initial deviations and saturation, improves lateral tracking and accelerates nominal-boundary re-entry, while the remaining executable-boundary exceedance indicates the need for conservative relaxation-budget selection in severe capability-limited cases. An additional Aerosonde-class 6-DoF engineering validation further showed that the outer-loop formation commands can be coupled to a representative fixed-wing rigid-body plant without trajectory divergence, although this validation does not constitute flight-test or hardware-in-the-loop evidence and does not show uniform dominance over all baselines in all tracking-error channels.

A limitation of this work is that the slow coordination layer is updated periodically. If the update period is too long or the environment changes rapidly, recovery coordination may be degraded. Future work will investigate event-triggered or self-triggered coordination mechanisms, as well as distributed formation recovery and obstacle-aware reconfiguration.

Author Contributions: Conceptualization, X.F. and H.C.; methodology, X.F.; software, X.F.; validation, X.F., H.C. and H.W.; formal analysis, X.F.; investigation, X.F.; resources, H.C.; data curation, X.F.; writing—original draft preparation, X.F.; writing—review and editing, H.C., H.W., X.X., W.W., T.H. and S.L.; visualization, X.F.; supervision, H.C.; project administration, H.C.; funding acquisition, H.C. All authors have read and agreed to the published version of the manuscript.

Funding: This research received no external funding.

Institutional Review Board Statement: Not applicable.

Informed Consent Statement: Not applicable.

Data Availability Statement: The datasets presented in this article are not readily available because they are part of an ongoing research project and are subject to confidentiality and project restrictions. The corresponding code for these datasets is also subject to the same restrictions. Access to certain data or code may be limited, as the authors are not permitted or authorized to disclose them at this stage. Requests for access should be directed to Email: by2015117@buaa.edu.cn; however, please note that some data or code may not be shared without appropriate authorization.

Conflicts of Interest: The authors declare no conflicts of interest.

Appendix A. Stability and Recoverability Analysis

This section analyzes the closed-loop properties of CAEBR. The analysis establishes that the executable boundary and the heading-support tube are forward invariant, all internal closed-loop signals remain bounded, and the executable boundary recovers toward the nominal deadline boundary whenever sufficient maneuvering capability is restored.

Appendix A.1. Lateral Recovery Priority Effect

Lemma A1. *Suppose* $|z_{\theta,i}| \le r_{\theta,i}$, $\gamma_{\omega,i} > 0$, *and* $\gamma_{\theta,i} > 0$. *If*

$$\rho_{y,i} > 0 \quad \text{or} \quad \sigma_{y,i} > 0, \tag{A1}$$

then, under the virtual-heading law in Equation (55), the priority-dependent terms generate an additional virtual-heading correction in the lateral-error-reducing direction. Consequently, under the local lateral inward-sector property of Lemma 1, the priority mechanism can strengthen the conservative inward lateral recovery effect whenever the turn-rate and heading-support margins remain nonzero.

Proof. Define the unsaturated argument in the virtual-heading law of Equation (55) as

$$\Theta_{v,i}(\pi_{y,i}) = -\bar{\theta}_i\big(1+\alpha_\theta \pi_{y,i}\big)\tanh\big(k_{y,i}(\hat{\chi}_{y,i})\zeta_{y,i}\big) - \beta_\theta \pi_{y,i}\tanh(\zeta_{y,i}). \tag{A2}$$

From Equation (53), if $\rho_{y,i} > 0$ or $\sigma_{y,i} > 0$, and $\gamma_{\omega,i}\gamma_{\theta,i} > 0$, then $\pi_{y,i} > 0$.

For $\zeta_{y,i} \neq 0$, since $k_{y,i}(\hat{\chi}_{y,i}) > 0$, we have

$$\operatorname{sgn}\big(\tanh\big(k_{y,i}(\hat{\chi}_{y,i})\zeta_{y,i}\big)\big) = \operatorname{sgn}(\zeta_{y,i}), \qquad \operatorname{sgn}\big(\tanh(\zeta_{y,i})\big) = \operatorname{sgn}(\zeta_{y,i}). \tag{A3}$$

Thus,

$$\operatorname{sgn}\left(\Theta_{v,i}(\pi_{y,i})\right) = -\operatorname{sgn}(\zeta_{y,i}) \tag{A4}$$

whenever the expression is nonzero. Moreover,

$$\begin{aligned} |\Theta_{v,i}(\pi_{y,i})| &= \bar{\theta}_i(1+\alpha_\theta \pi_{y,i})\left|\tanh\left(k_{y,i}(\widehat{\chi}_{y,i})\zeta_{y,i}\right)\right| + \beta_\theta \pi_{y,i}|\tanh(\zeta_{y,i})| \\ &\geq \bar{\theta}_i\left|\tanh\left(k_{y,i}(\widehat{\chi}_{y,i})\zeta_{y,i}\right)\right| = |\Theta_{v,i}(0)|. \end{aligned} \tag{A5}$$

Furthermore, for $\pi_{y,i} > 0$,

$$|\Theta_{v,i}(\pi_{y,i})| - |\Theta_{v,i}(0)| = \pi_{y,i}\left[\alpha_\theta \bar{\theta}_i\left|\tanh\left(k_{y,i}(\widehat{\chi}_{y,i})\zeta_{y,i}\right)\right| + \beta_\theta|\tanh(\zeta_{y,i})|\right] \geq 0. \tag{A6}$$

Therefore, before the outer saturation is reached, the priority variable increases the virtual-heading correction magnitude in the direction $-\operatorname{sgn}(\zeta_{y,i})$, which is the lateral-error-reducing direction required by Lemma 1. If the outer saturation is reached, the applied virtual-heading command remains bounded by

$$|\theta_{v,i}| \leq \bar{\theta}_{\max}. \tag{A7}$$

Therefore, under the local inward-sector property, the priority mechanism can strengthen the conservative inward lateral recovery effect whenever the turn-rate and heading-support margins remain nonzero. □

Appendix A.2. Closed-Loop Stability

Theorem A1. *Consider the closed-loop system composed of the fast-layer controller Equations (55)–(59), the slow coordination laws Equations (69) and (70), and the adaptive laws Equation (98). Suppose that the executable boundary has been initialized according to Equation (22) and satisfies Equation (23), so that*

$$|\check{e}_{x,i}(0)| < 1, \qquad |\check{e}_{y,i}(0)| < 1, \qquad |z_{\theta,i}(0)| < r_{\theta,i}. \tag{A8}$$

Assume that the actually applied slow-layer schedule, whether obtained from the optimizer or from the fallback rule, satisfies Equations (26) and (27) for all $t \geq 0$. Assume further that the longitudinal inward condition in Equation (A25) and the lateral executable-sector margin

$$\underline{c}_{y,i} > \bar{\Delta}_{y,i} \tag{A9}$$

hold on the considered operating interval. Under these admissible scheduling, projection initialization, and bounded equivalent-remainder assumptions, there exist controller parameters such that all closed-loop signals are bounded and

$$|\check{e}_{x,i}(t)| < 1, \qquad |\check{e}_{y,i}(t)| < 1, \qquad |z_{\theta,i}(t)| \leq r_{\theta,i}, \qquad \forall t \geq 0. \tag{A10}$$

Consequently, the longitudinal and lateral tracking errors remain inside the executable boundaries for all $t \geq 0$.

Proof. The equivalent residual remainders

Step 1: Bounded adaptive estimates and coordination variables.

By the projection initialization in Equation (30), the projection sets in Equation (101), and the projection-based adaptive laws in Equation (98), the adaptive estimates remain in their compact projection sets for all $t \geq 0$. Hence, $\hat{W}_{x,i}$ and $\hat{W}_{\theta,i}$ are bounded. Since the ideal weights are constant and belong to the corresponding compact analysis sets, the parameter estimation errors $\tilde{W}_{x,i}$ and $\tilde{W}_{\theta,i}$ are also bounded.

Moreover, by the admissible coordination design in Equations (26) and (27), the slow coordination variables and the executable-boundary variables are bounded and satisfy their admissible ranges for all $t \geq 0$. Therefore, the adaptive estimates, parameter estimation errors, slow coordination variables, and executable-boundary variables are bounded.

Step 2: Forward invariance of the heading-support tube.

Using the bounded turn-rate command in Equation (58), the heading-support error dynamics can be written as

$$\dot{z}_{\theta,i} = -k_{\theta,i}(\widehat{\chi}_{\theta,i}) \tanh(\lambda_\theta z_{\theta,i}) - \beta_z r_{\theta,i} \tanh\!\left(\frac{z_{\theta,i}}{r_{\theta,i}}\right) + \tilde{W}_{\theta,i}^\top \Phi_{\theta,i} + d_{\theta,i}^{\mathrm{eq}}, \tag{A11}$$

where $\tilde{W}_{\theta,i} = W_{\theta,i}^* - \hat{W}_{\theta,i}$. At the upper boundary $z_{\theta,i} = r_{\theta,i}$,

$$\begin{aligned} \dot{z}_{\theta,i} &\leq -k_{\theta,\min} \tanh(\lambda_\theta r_{\theta,i}) - \beta_z r_{\theta,i} \tanh(1) + \|\tilde{W}_{\theta,i}\| \|\Phi_{\theta,i}\| + \bar{d}_{\theta,i}^{\mathrm{eq}} \\ &\leq -k_{\theta,\min} \tanh(\lambda_\theta r_{\theta,i}) - \beta_z r_{\theta,i} \tanh(1) + \bar{\tilde{W}}_{\theta,i} \bar{\Phi}_\theta + \bar{d}_{\theta,i}^{\mathrm{eq}} < 0, \end{aligned} \tag{A12}$$

At the lower boundary $z_{\theta,i} = -r_{\theta,i}$,

$$\dot{z}_{\theta,i} \geq k_{\theta,\min} \tanh(\lambda_\theta r_{\theta,i}) + \beta_z r_{\theta,i} \tanh(1) - \bar{\tilde{W}}_{\theta,i} \bar{\Phi}_\theta - \bar{d}_{\theta,i}^{\mathrm{eq}} > 0. \tag{A13}$$

Thus, the vector field points strictly inward at both boundaries of the interval $[-r_{\theta,i}, r_{\theta,i}]$. Since $|z_{\theta,i}(0)| \leq r_{\theta,i}$, the heading-support tube is forward invariant.

Step 3: Longitudinal transformed-error boundedness and adaptive subsystem boundedness.

For $j \in \{x, y\}$, whenever $|\breve{e}_{j,i}| < 1$, direct differentiation of the transformed error yields

$$\dot{\zeta}_{j,i} = a_{j,i}(t) \dot{e}_{j,i} - b_{j,i}(t), \tag{A14}$$

where

$$a_{j,i}(t) := \frac{\kappa_j \operatorname{sech}^2(\kappa_j e_{j,i}(t))}{\mu_{j,i}^{\mathrm{act}}(t)\left(1 - \breve{e}_{j,i}^2(t)\right)}, \qquad b_{j,i}(t) := \frac{\dot{\mu}_{j,i}^{\mathrm{act}}(t)}{\mu_{j,i}^{\mathrm{act}}(t)} \frac{\breve{e}_{j,i}(t)}{1 - \breve{e}_{j,i}^2(t)}. \tag{A15}$$

By Equation (27), within the executable boundary we have

$$|\tanh(\kappa_j e_{j,i})| < \mu_{j,i}^{\mathrm{act}}(t) \leq \bar{\mu}_{j,i} < 1. \tag{A16}$$

Thus, $e_{j,i}$ remains in a finite interval over the maximal transformed-error interval. Since $|\dot{\mu}_{j,i}^{\mathrm{act}}|$ is bounded, the ratio $b_{j,i}/a_{j,i}$ is bounded. We therefore define

$$r_{j,i}(t) := \frac{b_{j,i}(t)}{a_{j,i}(t)}, \qquad |r_{j,i}(t)| \leq \bar{r}_{j,i}, \qquad j \in \{x, y\}. \tag{A17}$$

On the admissible domain, the longitudinal error dynamics can be written in the following analysis form

$$\dot{e}_{x,i} = -\left(1 - \alpha_v \pi_{y,i}\right)\left[k_{x,i}(\widehat{\chi}_{x,i}) + \beta_x\right] \tanh(\zeta_{x,i}) + \tilde{W}_{x,i}^\top \Phi_{x,i} + d_{x,i}^{\mathrm{eq}}, \tag{A18}$$

where $\tilde{W}_{x,i} = W_{x,i}^* - \hat{W}_{x,i}$.

Combining Equations (A14), (A17) and (A18) gives

$$\dot{\zeta}_{x,i} = a_{x,i}\Big[-\left(1 - \alpha_v \pi_{y,i}\right)\left(k_{x,i}(\widehat{\chi}_{x,i}) + \beta_x\right) \tanh(\zeta_{x,i}) + \tilde{W}_{x,i}^\top \Phi_{x,i} + d_{x,i}^{\mathrm{eq}} - r_{x,i}(t)\Big]. \tag{A19}$$

Consider the Lyapunov function candidate

$$V_{a,i} = \frac{1}{2}\zeta_{x,i}^2 + \frac{1}{2}z_{\theta,i}^2 + \frac{1}{2}\tilde{W}_{x,i}^\top \Gamma_x^{-1}\tilde{W}_{x,i} + \frac{1}{2}\tilde{W}_{\theta,i}^\top \Gamma_\theta^{-1}\tilde{W}_{\theta,i}. \tag{A20}$$

Because $\tilde{W} = W^* - \hat{W}$, we have

$$\dot{\tilde{W}}_{x,i} = -\dot{\hat{W}}_{x,i}, \qquad \dot{\tilde{W}}_{\theta,i} = -\dot{\hat{W}}_{\theta,i}. \tag{A21}$$

Using the projection property in Equation (102), the adaptive laws imply

$$\tilde{W}_{x,i}^\top \Gamma_x^{-1}\dot{\tilde{W}}_{x,i} \le -\tilde{W}_{x,i}^\top \Phi_{x,i} a_{x,i}\zeta_{x,i} + \sigma_x \tilde{W}_{x,i}^\top \hat{W}_{x,i}, \tag{A22}$$

and

$$\tilde{W}_{\theta,i}^\top \Gamma_\theta^{-1}\dot{\tilde{W}}_{\theta,i} \le -\tilde{W}_{\theta,i}^\top \Phi_{\theta,i} z_{\theta,i} + \sigma_\theta \tilde{W}_{\theta,i}^\top \hat{W}_{\theta,i}. \tag{A23}$$

Thus, the adaptive cross term in the longitudinal transformed-error channel is canceled.

Define

$$C_{x,i} := (1-\alpha_v)\big(k_{x,\min} + \beta_x\big), \qquad D_{x,i} := \bar{d}_{x,i}^{\mathrm{eq}} + \bar{r}_{x,i}. \tag{A24}$$

The longitudinal gain condition is imposed as

$$C_{x,i} > D_{x,i}. \tag{A25}$$

Since $0 \le \pi_{y,i} \le 1$, $0 < \alpha_v < 1$, and $k_{x,i}(\hat{\chi}_{x,i}) \ge k_{x,\min}$, it follows that

$$\big(1 - \alpha_v \pi_{y,i}\big)\big(k_{x,i}(\hat{\chi}_{x,i}) + \beta_x\big) \ge C_{x,i}. \tag{A26}$$

Using Equations (A19)–(A26), one obtains

$$\begin{aligned} \zeta_{x,i}\dot{\zeta}_{x,i} + \tilde{W}_{x,i}^\top \Gamma_x^{-1}\dot{\tilde{W}}_{x,i} \le{}& -a_{x,i}C_{x,i}\zeta_{x,i}\tanh(\zeta_{x,i}) + a_{x,i}|\zeta_{x,i}|D_{x,i} \\ & + \sigma_x \tilde{W}_{x,i}^\top \hat{W}_{x,i}. \end{aligned} \tag{A27}$$

Since

$$\zeta_{x,i}\tanh(\zeta_{x,i}) = |\zeta_{x,i}|\tanh(|\zeta_{x,i}|), \tag{A28}$$

Equation (A27) becomes

$$\begin{aligned} \zeta_{x,i}\dot{\zeta}_{x,i} + \tilde{W}_{x,i}^\top \Gamma_x^{-1}\dot{\tilde{W}}_{x,i} \le{}& -a_{x,i}|\zeta_{x,i}|\big[C_{x,i}\tanh(|\zeta_{x,i}|) - D_{x,i}\big] \\ & + \sigma_x \tilde{W}_{x,i}^\top \hat{W}_{x,i}. \end{aligned} \tag{A29}$$

If the longitudinal gain condition in Equation (A25) holds, i.e., $C_{x,i} > D_{x,i}$, then there exists a constant $\varepsilon_{x,i} > 0$ such that

$$D_{x,i} + \varepsilon_{x,i} < C_{x,i}. \tag{A30}$$

Define

$$\zeta_{x,i}^\star = \operatorname{artanh}\left(\frac{D_{x,i} + \varepsilon_{x,i}}{C_{x,i}}\right). \tag{A31}$$

Then, whenever $|\zeta_{x,i}| \ge \zeta_{x,i}^\star$,

$$C_{x,i}\tanh(|\zeta_{x,i}|) - D_{x,i} \ge \varepsilon_{x,i}. \tag{A32}$$

Consequently, outside the compact set $|\zeta_{x,i}| < \zeta^\star_{x,i}$, the longitudinal transformed-error dynamics admit an inward dissipative component:

$$\zeta_{x,i}\dot{\zeta}_{x,i} \leq -a_{x,i}\varepsilon_{x,i}|\zeta_{x,i}| + \sigma_x \tilde{W}_{x,i}^\top \hat{W}_{x,i}. \tag{A33}$$

For the leakage term, using $\hat{W} = W^* - \tilde{W}$ and Young's inequality gives

$$\sigma_x \tilde{W}_{x,i}^\top \hat{W}_{x,i} \leq -\frac{\sigma_x}{2}\|\tilde{W}_{x,i}\|^2 + \frac{\sigma_x}{2}\|W^*_{x,i}\|^2. \tag{A34}$$

Similarly,

$$\sigma_\theta \tilde{W}_{\theta,i}^\top \hat{W}_{\theta,i} \leq -\frac{\sigma_\theta}{2}\|\tilde{W}_{\theta,i}\|^2 + \frac{\sigma_\theta}{2}\|W^*_{\theta,i}\|^2. \tag{A35}$$

For the heading-support channel, Equations (A11) and (A23) yield

$$\begin{aligned} z_{\theta,i}\dot{z}_{\theta,i} + \tilde{W}_{\theta,i}^\top \Gamma_\theta^{-1}\dot{\tilde{W}}_{\theta,i} \leq{} & -k_{\theta,\min} z_{\theta,i}\tanh(\lambda_\theta z_{\theta,i}) \\ & - \beta_z r_{\theta,i} z_{\theta,i}\tanh\left(\frac{z_{\theta,i}}{r_{\theta,i}}\right) + |z_{\theta,i}| \bar{d}^{\mathrm{eq}}_{\theta,i} \\ & + \sigma_\theta \tilde{W}_{\theta,i}^\top \hat{W}_{\theta,i}. \end{aligned} \tag{A36}$$

Since $z_{\theta,i}$ remains within the invariant tube by Step 2 and the projection terms satisfy the bounds in Equations (A34) and (A35), the variables $z_{\theta,i}$, $\tilde{W}_{x,i}$, and $\tilde{W}_{\theta,i}$ remain bounded. Moreover, $\zeta_{x,i}$ is ultimately confined to a compact set determined by $C_{x,i}$, $D_{x,i}$, the boundary variation, and the leakage bounds. Therefore, $\zeta_{x,i}$, $z_{\theta,i}$, $\tilde{W}_{x,i}$, and $\tilde{W}_{\theta,i}$ are uniformly ultimately bounded.

Step 4: Boundedness of the lateral transformed error.

By Step 2, $|z_{\theta,i}(t)| \leq r_{\theta,i}$ for all $t \geq 0$. Under the admissible lateral executable-sector condition in Lemma 1, the lateral transformed-error channel satisfies

$$\zeta_{y,i}\dot{\zeta}_{y,i} \leq -\underline{c}_{y,i}\zeta_{y,i}\tanh(\zeta_{y,i}) + |\zeta_{y,i}|\bar{\Delta}_{y,i}. \tag{A37}$$

Consider the Lyapunov function candidate

$$V_{y,i} = \frac{1}{2}\zeta_{y,i}^2. \tag{A38}$$

Then

$$\dot{V}_{y,i} \leq -\underline{c}_{y,i}\zeta_{y,i}\tanh(\zeta_{y,i}) + |\zeta_{y,i}|\bar{\Delta}_{y,i}. \tag{A39}$$

Using

$$\zeta_{y,i}\tanh(\zeta_{y,i}) = |\zeta_{y,i}|\tanh(|\zeta_{y,i}|), \tag{A40}$$

we obtain

$$\dot{V}_{y,i} \leq -|\zeta_{y,i}|\Big[\underline{c}_{y,i}\tanh(|\zeta_{y,i}|) - \bar{\Delta}_{y,i}\Big]. \tag{A41}$$

If the lateral inward-sector margin condition

$$\underline{c}_{y,i} > \bar{\Delta}_{y,i} \tag{A42}$$

holds, then there exists a constant $\varepsilon_{y,i} > 0$ such that

$$\bar{\Delta}_{y,i} + \varepsilon_{y,i} < \underline{c}_{y,i}. \tag{A43}$$

Define

$$\zeta^\star_{y,i} = \operatorname{artanh}\left(\frac{\bar{\Delta}_{y,i} + \varepsilon_{y,i}}{\underline{c}_{y,i}}\right). \tag{A44}$$

Whenever $|\zeta_{y,i}| \geq \zeta^{\star}_{y,i}$,

$$\underline{c}_{y,i} \tanh(|\zeta_{y,i}|) - \bar{\Delta}_{y,i} \geq \varepsilon_{y,i}. \tag{A45}$$

Therefore,

$$\dot{V}_{y,i} \leq -\varepsilon_{y,i}|\zeta_{y,i}| < 0, \qquad \text{whenever } |\zeta_{y,i}| \geq \zeta^{\star}_{y,i}. \tag{A46}$$

Therefore, $\zeta_{y,i}$ is bounded for all $t \geq 0$.

Step 5: Forward invariance of the executable boundary.

The transformed coordinates $\zeta_{x,i}$ and $\zeta_{y,i}$ are well defined provided that

$$|\check{e}_{x,i}| < 1, \qquad |\check{e}_{y,i}| < 1. \tag{A47}$$

Let $[0, T_{\max})$ be the maximal interval on which these inequalities hold. On this interval, Steps 3 and 4 show that $\zeta_{x,i}$ and $\zeta_{y,i}$ remain bounded. Since

$$\check{e}_{j,i}(t) = \tanh(\zeta_{j,i}(t)), \qquad j \in \{x, y\}, \tag{A48}$$

boundedness of $\zeta_{j,i}$ implies

$$|\check{e}_{j,i}(t)| < 1 \tag{A49}$$

for all finite $t < T_{\max}$. Hence, neither transformed boundary can be reached in finite time. Therefore, $T_{\max} = \infty$, and

$$|h_j(e_{j,i}(t))| < \mu^{\mathrm{act}}_{j,i}(t), \qquad j \in \{x, y\}, \qquad \forall t \geq 0. \tag{A50}$$

Step 6: Boundedness of internal closed-loop signals and conditional recovery of the nominal boundary.

From Step 5,

$$|h_j(e_{j,i}(t))| < \mu^{\mathrm{act}}_{j,i}(t) \leq \bar{\mu}_{j,i} < 1. \tag{A51}$$

Since $h_j(e) = \tanh(\kappa_j e)$ is invertible and strictly increasing, the tracking errors are bounded:

$$|e_{j,i}(t)| < \frac{1}{\kappa_j} \operatorname{artanh}(\bar{\mu}_{j,i}), \qquad j \in \{x, y\}. \tag{A52}$$

By Step 2, $z_{\theta,i}$ remains within the heading-support tube. The virtual-heading signal $\theta_{v,i}$ is bounded by the outer saturation in Equation (55). Since the filter is stable and driven by a bounded input, ψ_i is bounded. Since $z_{\theta,i} = \psi_i - \eta_i$, boundedness of $z_{\theta,i}$ and ψ_i implies boundedness of the relative heading η_i.

The applied inputs v_i and ω_i are bounded by the saturation operators. The unsaturated commands are bounded by construction on the admissible domain. The slow-layer variables $\delta_{x,i}$, $\delta_{y,i}$, $\sigma_{y,i}$, and $\Delta\bar{\theta}_i$ are bounded by the admissible coordination design in Equations (26) and (27). The adaptive weights, parameter estimation errors, adaptive residual estimates, residual-load indicators, estimated capability indices, and recovery priority are bounded by Step 1 and their saturation definitions. Therefore, all internal closed-loop signals, tracking errors, transformed errors, adaptive weights, coordination variables, and control inputs remain bounded.

It remains to prove conditional recovery of the nominal boundary. Suppose that after some time t_r, the estimated maneuvering capability remains sufficient and the slow coordinator selects admissible recovery actions satisfying, for some $0 < \underline{\lambda}_{\delta,j} < \lambda_{\delta,j}$,

$$v_{\delta,j,i}(t) \leq -\bar{c}_{\delta,j} + (\lambda_{\delta,j} - \underline{\lambda}_{\delta,j})\delta_{j,i}(t), \qquad c_{\delta,j}(1 - \widehat{\chi}_{j,i}) \leq \bar{c}_{\delta,j}. \tag{A53}$$

Then, from the relaxation dynamics in Equation (69), we have

$$\dot{\delta}_{j,i}(t) \leq -\underline{\lambda}_{\delta,j}\delta_{j,i}(t), \qquad j \in \{x, y\}, \tag{A54}$$

in the projected-vector-field sense. Direct integration yields

$$\delta_{x,i}(t) \leq \delta_{x,i}(t_r)e^{-\underline{\lambda}_{\delta,x}(t-t_r)}, \qquad \delta_{y,i}(t) \leq \delta_{y,i}(t_r)e^{-\underline{\lambda}_{\delta,y}(t-t_r)} \tag{A55}$$

for all $t \geq t_r$. Therefore,

$$\delta_{x,i}(t) \to 0, \qquad \delta_{y,i}(t) \to 0. \tag{A56}$$

Since

$$\mu_{j,i}^{\text{act}}(t) = \mu_{j,i}^{\text{nom}}(t) + \delta_{j,i}(t), \qquad j \in \{x, y\},$$

the executable boundary asymptotically recovers the nominal deadline boundary:

$$\mu_{j,i}^{\text{act}}(t) - \mu_{j,i}^{\text{nom}}(t) \to 0, \qquad j \in \{x, y\}. \tag{A57}$$

Moreover, by forward invariance,

$$|h_j(e_{j,i}(t))| < \mu_{j,i}^{\text{nom}}(t) + \delta_{j,i}(t). \tag{A58}$$

If the nominal deadline boundary satisfies

$$\mu_{j,i}^{\text{nom}}(t) \to \mu_{j,i}^{\infty}, \tag{A59}$$

then

$$\limsup_{t\to\infty} |h_j(e_{j,i}(t))| \leq \mu_{j,i}^{\infty}. \tag{A60}$$

Since $h_j(e) = \tanh(\kappa_j e)$ is strictly increasing and invertible,

$$\limsup_{t\to\infty} |e_{j,i}(t)| \leq \frac{1}{\kappa_j}\operatorname{artanh}(\mu_{j,i}^{\infty}) = r_{j,i}. \tag{A61}$$

This completes the proof. □

Theorem A1 shows that the executable boundary remains invariant when the boundary schedule and available input authority satisfy the inward conditions used in the proof. The nominal boundary is recovered conditionally after sufficient capability returns and the relaxation variables decay to zero.

References

1. Javed, S.; Hassan, A.; Ahmad, R.; Ahmed, W.; Ahmed, R.; Saadat, A.; Guizani, M. State-of-the-Art and Future Research Challenges in UAV Swarms. *IEEE Internet Things J.* **2024**, *11*, 19023–19045. https://doi.org/10.1109/JIOT.2024.3364230.
2. Rinaldi, M.; Wang, S.; Geronel, R.S.; Primatesta, S. Application of Task Allocation Algorithms in Multi-UAV Intelligent Transportation Systems: A Critical Review. *Big Data Cogn. Comput.* **2024**, *8*, 177. https://doi.org/10.3390/bdcc8120177.
3. Wang, G.; Lv, X.; Cui, L.; Yan, X. The Methods of Task Pre-allocation and Reallocation for Multi-UAV Cooperative Reconnaissance Mission. *IET Collab. Intell. Manuf.* **2023**, *5*, e12090. https://doi.org/10.1049/cim2.12090.

4. Mirzaee Kahagh, A.; Pazooki, F.; Etemadi Haghighi, S.; Asadi, D. Real-Time Formation Control and Obstacle Avoidance Algorithm for Fixed-Wing UAVs. *Aeronaut. J.* **2022**, *126*, 2111–2133. https://doi.org/10.1017/aer.2022.9.
5. Yang, J.; Thomas, A.G.; Singh, S.; Baldi, S.; Wang, X. A Semi-Physical Platform for Guidance and Formations of Fixed-Wing Unmanned Aerial Vehicles. *Sensors* **2020**, *20*, 1136. https://doi.org/10.3390/s20041136.
6. Yan, J.; Yu, Y.; Wang, X. Distance-Based Formation Control for Fixed-Wing UAVs with Input Constraints: A Low Gain Method. *Drones* **2022**, *6*, 159. https://doi.org/10.3390/drones6070159.
7. Tian, L.; Wang, X.; Chen, H. Heterogeneous Formation Tracking for Fixed-Wing UAVs and Nonholonomic UGVs with Different Asymmetric Constraints. *IEEE Trans. Veh. Technol.* **2025**, *74*, 13350–13360. https://doi.org/10.1109/TVT.2025.3558892.
8. Sui, L.; Jin, Z. Learning-Based Finite-Time Distributed Formation Control for Fixed-Wing Unmanned Aerial Vehicles. *Int. J. Control Autom. Syst.* **2024**, *22*, 3191–3201. https://doi.org/10.1007/s12555-024-0207-7.
9. He, L.; Dong, W. Distributed Adaptive Consensus Tracking Control for Heterogeneous Nonlinear Multi-Agent Systems. *ISA Trans.* **2022**, *130*, 177–183. https://doi.org/10.1016/j.isatra.2022.03.022.
10. Wang, Z.; Zhu, Y.; Chen, X.; Su, C.-Y.; Yang, F. Finite-Iterative Learning Consensus Formation Control for Multi-Agent Systems Under Double-Terminal Switching Topologies. *IEEE Trans. Netw. Sci. Eng.* **2025**, *12*, 803–813. https://doi.org/10.1109/TNSE.2024.3519560.
11. Qian, D.; Xi, Y. Leader–Follower Formation Maneuvers for Multi-Robot Systems via Derivative and Integral Terminal Sliding Mode. *Appl. Sci.* **2018**, *8*, 1045. https://doi.org/10.3390/app8071045.
12. Liu, Z.-Q.; Ge, X.; Xie, H.; Han, Q.-L.; Zheng, J.; Wang, Y.-L. Secure Leader–Follower Formation Control of Networked Mobile Robots Under Replay Attacks. *IEEE Trans. Ind. Inform.* **2024**, *20*, 4149–4159. https://doi.org/10.1109/TII.2023.3313651.
13. Wang, J.; Hu, Z.; Zhang, H. Multiple-AUV Formation Control with a Collision Avoidance Algorithm Based on a Virtual Structure and an Improved Artificial Potential Field Method. *Meas. Sci. Technol.* **2025**, *36*, 116203. https://doi.org/10.1088/1361-6501/ae1b2b.
14. Yu, H.; Ning, L. Coordinated Obstacle Avoidance of Multi-AUV Based on Improved Artificial Potential Field Method and Consistency Protocol. *J. Mar. Sci. Eng.* **2023**, *11*, 1157. https://doi.org/10.3390/jmse11061157.
15. Liu, Y.; Chen, C.; Wang, Y.; Zhang, T.; Gong, Y. A Fast Formation Obstacle Avoidance Algorithm for Clustered UAVs Based on Artificial Potential Field. *Aerosp. Sci. Technol.* **2024**, *147*, 108974. https://doi.org/10.1016/j.ast.2024.108974.
16. Li, W.; Chen, X.; Ji, L.; Song, J.; Li, S. Finite-Time Formation Control for Multi-Agent Systems with Dynamic Leader and Input Saturation. *Electron. Res. Arch.* **2025**, *33*, 7699–7716. https://doi.org/10.3934/era.2025340.
17. Li, Y.; Zhang, P.; Wang, Z.; Rong, D.; Niu, M.; Liu, C. Multi-UAV Obstacle Avoidance and Formation Control in Unknown Environments. *Drones* **2024**, *8*, 714. https://doi.org/10.3390/drones8120714.
18. Heintz, C.; Bailey, S.C.C.; Hoagg, J.B. Formation Control for Autonomous Fixed-Wing Air Vehicles with Strict Speed Constraints. *Auton. Robot.* **2023**, *47*, 1299–1323. https://doi.org/10.1007/s10514-023-10126-4.
19. Li, H.; Chen, H.; Wang, X. Affine Formation Tracking Control of Unmanned Aerial Vehicles. *Front. Inf. Technol. Electron. Eng.* **2022**, *23*, 909–919. https://doi.org/10.1631/FITEE.2100109.
20. Yu, Y.; Chen, J.; Zheng, Z.; Yuan, J. Distributed Finite-Time ESO-Based Consensus Control for Multiple Fixed-Wing UAVs Subjected to External Disturbances. *Drones* **2024**, *8*, 260. https://doi.org/10.3390/drones8060260.
21. Liu, Z.; Wang, X.; Shen, L.; Zhao, S.; Cong, Y.; Li, J.; Yin, D.; Jia, S.; Xiang, X. Mission-Oriented Miniature Fixed-Wing UAV Swarms: A Multilayered and Distributed Architecture. *IEEE Trans. Syst. Man Cybern. Syst.* **2022**, *52*, 1588–1602. https://doi.org/10.1109/TSMC.2020.3033935.
22. Yang, Z.; Luo, D.; Guo, Z.; Xu, Y. Adaptive Predefined-Time Path-Following Control for Fixed-Wing UAV Formations with Prescribed Performance. *Appl. Math. Model.* **2025**, *147*, 116173. https://doi.org/10.1016/j.apm.2025.116173.
23. Meng, B.; Zhang, K.; Jiang, B. Fixed-Time Optimal Fault-Tolerant Formation Control with Prescribed Performance for Fixed-Wing UAVs Under Dual Faults. *IEEE Trans. Signal Inf. Process. Netw.* **2023**, *9*, 875–887. https://doi.org/10.1109/TSIPN.2023.3341406.
24. Li, S.; Wang, S.; Zhang, Y.; Wang, X.; Zhang, Y.; Wu, W.; Chen, R.; Mu, R. Distributed Bearing-Based Fault-Tolerant Formation Control of Fixed-Wing UAV Swarm with Prescribed Performance. *Aerosp. Sci. Technol.* **2026**, *168*, 110897. https://doi.org/10.1016/j.ast.2025.110897.
25. Yang, W. Distributed Robust Adaptive Practical Finite-Time Formation Tracking Control of Fixed-Wing UAVs. *Aerosp. Sci. Technol.* **2025**, *166*, 110552. https://doi.org/10.1016/j.ast.2025.110552.
26. Zheng, J.; Zhao, S.; Wang, X.; Tang, J.; Zuo, Z. Prescribed-Time Maneuvering Target Closing for Multiple Fixed-Wing UAVs. *IEEE Trans. Veh. Technol.* **2024**, *73*, 12614–12624. https://doi.org/10.1109/TVT.2024.3394003.
27. Lou, G.; Lv, M. Prescribed-Time Formation Tracking Control of Fixed-Wing UAVs with Disturbance and Failures. *Machines* **2026**, *14*, 543. https://doi.org/10.3390/machines14050543.
28. Wang, Q.; Dong, X.; Chen, Z.; Lian, Z.; Lü, J. Finite-Time Formation Tracking for Heterogeneous Euler–Lagrange Systems with an Uncertain Leader. *Automatica* **2025**, *176*, 112268. https://doi.org/10.1016/j.automatica.2025.112268.

29. Chang, S.; Wang, Y.; Zuo, Z. Fixed-Time Formation-Containment Control for Uncertain Multi-Agent Systems with Varying Gain Extended State Observer. *Inf. Sci.* **2022**, *612*, 759–779. https://doi.org/10.1016/j.ins.2022.08.096.
30. Liu, Z.; Gong, Q.; Hu, X.; Zhu, G.; Guo, S.; Ma, B.; Li, X. Practical Fixed-Time Formation Control with Disturbance Rejection for Marine Vehicles Under Input Saturation. *ISA Trans.* **2025**, *164*, 100–115. https://doi.org/10.1016/j.isatra.2025.05.032.
31. Hou, T.; Bi, W.; Huang, Z.; Yang, P.; Zhang, A. Time-Varying Formation Tracking for Multi-Agent Systems Based on Prescribed-Time Control. *Proc. Inst. Mech. Eng. Part I J. Syst. Control Eng.* **2025**, *239*, 1093–1106. https://doi.org/10.1177/09596518241309128.
32. Yang, T.; Zhang, P.; Chen, H. Distributed Prescribed-Time Leader–Follower Formation Control of Surface Vehicles with Unknowns and Input Saturation. *ISA Trans.* **2023**, *134*, 16–27. https://doi.org/10.1016/j.isatra.2022.07.033.
33. Ilchmann, A.; Ryan, E.P.; Townsend, P. Tracking Control with Prescribed Transient Behaviour for Systems of Known Relative Degree. *Syst. Control Lett.* **2006**, *55*, 396–406. https://doi.org/10.1016/j.sysconle.2005.09.002.
34. Berger, T.; Ilchmann, A.; Ryan, E.P. Funnel Control of Nonlinear Systems. *Math. Control Signals Syst.* **2021**, *33*, 151–194. https://doi.org/10.1007/s00498-021-00277-z.
35. Bechlioulis, C.P.; Rovithakis, G.A. Robust Adaptive Control of Feedback Linearizable MIMO Nonlinear Systems with Prescribed Performance. *IEEE Trans. Autom. Control* **2008**, *53*, 2090–2099. https://doi.org/10.1109/TAC.2008.929402.
36. Zhao, L.; Hu, C.; Yu, J.; Wen, S.; Huang, T. Fixed/Preassigned-Time Bipartite Output Regulation of Heterogeneous Multiagent Systems. *IEEE Trans. Cybern.* **2026**, *56*, 1541–1554. https://doi.org/10.1109/TCYB.2025.3628610.
37. Fei, Y.; Shi, P.; Lim, C.C. Neural-Based Formation Control of Uncertain Multi-Agent Systems with Actuator Saturation. *Nonlinear Dyn.* **2022**, *108*, 3693–3709. https://doi.org/10.1007/s11071-022-07434-2.
38. Li, Y.; Dong, S.; Li, K. Command Filter Adaptive Fuzzy Formation Asymptotic Tracking Control for Nonholonomic Multirobot Systems with Multiple Constraints. *IEEE Trans. Syst. Man Cybern. Syst.* **2024**, *54*, 1936–1947. https://doi.org/10.1109/TSMC.2023.3331353.
39. Dun, A.; Wang, R.; Lei, F.; Yang, Y. Dynamic Surface Control for Formation Control of Quadrotors with Input Constraints and Disturbances. T*Ransactions Inst. Meas. Control* **2022**, *44*, 2500–2510. https://doi.org/10.1177/01423312221085391.
40. Li, H.; Deng, H.; Li, M. Co-Design of Anti-Windup Compensator and a Novel Saturation-Based Dynamic Event-Triggered Mechanism for Asymmetric Saturated System. *Int. J. Control Autom. Syst.* **2024**, *22*, 537–547. https://doi.org/10.1007/s12555-022-0504-y.
41. Luo, Z.; Zhu, B.; Zheng, J.; Zheng, Z. Robust Distributed Model Predictive Control for Formation Tracking of Nonholonomic Vehicles. *IEEE/CAA J. Autom. Sin.* **2024**, *11*, 560–562. https://doi.org/10.1109/JAS.2023.123732.
42. Wang, S.; Wang, Y.; Miao, Z.; Wang, X.; He, W. Dual Model Predictive Control of Multiple Quadrotors With Formation Maintenance and Collision Avoidance. *IEEE Trans. Ind. Electron.* **2024**, *71*, 16037–16046. https://doi.org/10.1109/TIE.2024.3379663.
43. Wen, G.; Lam, J.; Fu, J.; Wang, S. Distributed MPC-Based Robust Collision Avoidance Formation Navigation of Constrained Multiple USVs. *IEEE Trans. Intell. Veh.* **2024**, *9*, 1804–1816. https://doi.org/10.1109/TIV.2023.3315367.
44. Qi, G.; Dong, Y.; Feng, J.; Zhu, C.; Yan, Y.; Li, F.; Zhao, D. Robust Model Predictive Control for the Beam-Pumping Unit Dynamic Liquid Level Stabilization. *Processes* **2026**, *14*, 1232. https://doi.org/10.3390/pr14081232.
45. Liu, Y.; Zhou, Y.; Su, S.; Xun, J.; Tang, T. Control Strategy for Stable Formation of High-Speed Virtually Coupled Trains with Disturbances and Delays. *Comput.-Aided Civ. Infrastruct. Eng.* **2023**, *38*, 621–639. https://doi.org/10.1111/mice.12873.
46. Wang, J.-W.; Wang, F.; Wu, H.-N.; Liu, Z.-Y. Safe RL-Based Adaptive Cooperative Game Control of Wing Deformation and Flight State Tracking for Morphing Hypersonic Vehicles. *IEEE Trans. Aerosp. Electron. Syst.* **2025**, *61*, 10826–10838. https://doi.org/10.1109/TAES.2025.3560610.
47. Yang, T.; Wu, H.-N.; Wang, J.-W. cc-DRL: A Convex Combined Deep Reinforcement Learning Flight Control Design of a Morphing Quadrotor. *IEEE Trans. Cybern.* **2025**, *55*, 4554–4566. https://doi.org/10.1109/TCYB.2025.3580074.
48. Guo, Y.; Wang, Z.; Li, T. Event-Triggered Formation Control for Fixed-Wing UAVs Under Compound Disturbances and Deception Attacks. *Arab. J. Sci. Eng.* **2026**. https://doi.org/10.1007/s13369-026-11098-0.
49. Wang, S.; Han, T.; Xiao, B.; Zhan, X.-S.; Yan, H. Practical Predefined-Time Formation Tracking of MASVs with Lumped Uncertainties via Estimator-Based Adaptive Fuzzy Control Algorithm. *IEEE Trans. Veh. Technol.* **2025**, *74*, 8797–8807. https://doi.org/10.1109/TVT.2025.3540770.
50. Qiao, Y.; Li, S.; Li, S. RNN Online Learning-Based Fixed-Time Prescribed Performance Formation Control for Networked Heterogeneous HFV Under Event-Triggered Communication. *IEEE Trans. Aerosp. Electron. Syst.* **2025**, *61*, 11364–11381. https://doi.org/10.1109/TAES.2025.3566683.
51. Wu, H.-Y.; Liu, Q.; Park, J.H. Observer-Based Secure Consensus for Multiagent Systems Under Multimode DoS Attacks with Application to Power System. *IEEE Trans. Cybern.* **2025**, *55*, 1032–1044. https://doi.org/10.1109/TCYB.2025.3528200.
52. Şekercioğlu, P.; Sarras, I.; Loría, A.; Panteley, E.; Marzat, J. Leader-Follower and Leaderless Bipartite Formation-Consensus over Undirected Coopetition Networks and Under Proximity and Collision-Avoidance Constraints. *Int. J. Control* **2025**, *98*, 642–656. https://doi.org/10.1080/00207179.2024.2354845.

53. Li, H.; Hu, J.; Zhou, Q.; Ghosh, B.K. Safe Formation Control of Multiple Unmanned Aerial Vehicles: Control Design and Safety-Stability Analysis. *Control Theory Technol.* **2024**, *22*, 442–454. https://doi.org/10.1007/s11768-024-00209-7.
54. Khaledi, M.; Kiumarsi, B. Data-Driven Distributed Safe Control Design for Multi-Agent Systems. *Int. J. Adapt. Control Signal Process.* **2026**, *40*, 137–150. https://doi.org/10.1002/acs.4088.